Late early Paleozoic continental collision on the northern margin of the Central Qilian Block, NE Tibetan Plateau: Evidence from a two-stage tectono–metamorphic event

Yi Sun[a], Manlan Niu[a*], Zhen Yan[b], Richard M. Palin[c], Chen Li[a], Xiucai Li[a], Xiaoyu Yuan[a]

[a] School of Resources and Environmental Engineering, Hefei University of Technology, Hefei 230009, China

[b] Institute of Geology, Chinese Academy of Geological Sciences, Beijing, China

[c] Department of Earth Sciences, University of Oxford, South Parks Road, Oxford, OX1 3AN, UK

*Corresponding Author: Manlan Niu

Submission to ***Journal of Asian Earth Sciences***

Abstract

The central part of the Qilian orogenic belt (QOB) on the NE Tibetan Plateau is known as the Central Qilian Block (CQB), and research on deformation and metamorphism of CQB improves our understanding of the tectonic evolution of the QOB, which makes up an important part of the continental crust in eastern Asia. Here we present the results of thermobarometric calculation and geochronological analyses for deformed metamorphic rocks on the northern margin of the CQB, and these new datasets provide a record of the continental collision of the CQB. Macrostructures and microstructures indicate that the CQB underwent dextral ductile deformation. C-axis fabrics and dynamic recrystallisation of quartz indicate that deformation took place at temperatures of 400–500 °C. In contrast, phase equilibrium modelling suggests that the region underwent *HT–MP* metamorphism along a clockwise *P–T* path, with peak conditions of ~740 °C and ~7.2 kbar. Zircon U–Pb ages obtained from the zircon rims indicate the *HT–MP* metamorphism took place at 452–449 Ma. The results of petrographic analyses indicate changes in the rims of the garnet porphyroblasts due to late ductile deformation, which suggests that the ductile shearing took place after the *HT–MP* metamorphism. The records of different temperatures of metamorphism and deformation are consistent with multi-stage metamorphism–deformation. Together with the results of previous research on the metamorphism, magmatism, and deformation in the CQB, our new datasets confirm that the *HT–MP* metamorphism and ductile deformation of the CQB were developed during the collision of the CQB and the Alxa Block.

Keywords Ductile shear belt, Proto-Tethys Ocean, continental collision, Qilian orogenic belt

1 Introduction

The supercontinent Rodinia started to break up between 750 and 600 Ma, probably as the result of a super-mantle plume event (Cawood et al., 2007; Zhao et al., 2012, 2018 and references therein), and this led to the opening of several oceans. One of these, the Proto-Tethys Ocean, separated the South China, North China, Alxa, Qaidam, Tarim and Central Qilian blocks from other East Asian blocks, which were located at the margins of Australia and India (Zhao et al., 2018 and references therein). From *ca.* 530 Ma, the Proto-Tethys Ocean started to shrink and close, leading to the first assembly of nearly all East Asian blocks (*e.g.*, the Tarim, Qaidam, Alxa and Central Qilian blocks), which were juxtaposed at the northern margin of Greater Gondwana (*e.g.*, Li et al., 2018a; Zhang et al., 2017; Zhao et al., 2020; Yu et al., 2021; Fig. 1a). Investigating the evolution of these continental blocks can therefore provide reliable constraints on the supercontinent cycle from Rodinia to Gondwana.

The Qilian orogenic belt (QOB), which makes up the central part of the Central China orogenic belt on the NE Tibetan Plateau, is one of the most important suture zones in eastern Asia (Xiao et al., 2009; Dong et al., 2021). The QOB was formed by oceanic plate subduction and the amalgamation of several small continental crustal crusts during the early Paleozoic (Fig. 1a; *e.g.*, Xiao et al., 2009; Yin et al., 2010; Gehrels et al., 2011; Fu et al., 2018; Yan et al., 2019a, b, 2021; Yu et al., 2019a, b, 2021; Dong et al., 2021). The Central Qilian Block (CQB), which was one of the microcontinents in the Proto-Tethys Ocean, is an integral part of the QOB. The CQB is dominated by gneiss, schist, amphibolite, graphitic marble, and migmatite (BGMR-GP, 1989; BGMR-QP, 1991; Fig. 1b). The Proto-Tethys

Ocean was separated into two oceanic branches by the CQB, and these branches were the North Qilian Ocean in the north and the South Qilian Ocean in the south. The North Qilian Ocean was sandwiched between the Alxa Block and the CQB. In response to multiple subduction- and collision-related processes during the closure of the North Qilian Ocean, numerous stages of deformation and metamorphism took place in the CQB and NQB (*e.g.,* Zhang et al., 1997; Qi et al., 2004; Xiao et al., 2009; Song et al., 2013, 2019; Li et al., 2017, 2018; Fu et al., 2020; Yan et al., 2021; Yu et al., 2021). A large E–W trending strike-slip ductile shear belt developed along the northern margin of this block, and this shearing was related to the evolution of the North Qilian Ocean but has not yet been studied systematically (Qi et al., 2004; Xiao et al., 2009; Tung et al., 2013; Xu et al., 2016). Many studies have been undertaken on the early stage (*ca.* 500 Ma) *HT–LP* metamorphism related to the subduction of the Proto-Tethyan oceanic plate in this region, and these studies have provided information on the *P–T* conditions of this metamorphism (*e.g.*, Wan et al., 2010; Tung et al., 2013; Peng et al., 2017a; Yu et al., 2019a, 2021). However, little information has been provided for the late-stage metamorphism and deformation that was related to the closure of the Proto-Tethys Ocean during the early Paleozoic, and this restricts us from making reasonable reconstructions of the history of the CQB and does not help our understanding of the evolution of the QOB.

In this contribution, we place new constraints on the *P–T* conditions of metamorphism and deformation in the area by presenting the results of geologic mapping, structural analysis, geochronological analysis, mineralogy, geochemistry

and geothermobarometry of metamorphic rocks along the northern margin of the CQB. Our integrated study of the multiple episodes of metamorphism and deformation during the late early Paleozoic has allowed us to rebuild the tectonic history of the CQB and improve our understanding of the evolution of the QOB.

2 Geological setting

The QOB was formed by multiple subduction and collision events related to the evolution of the Proto-Tethys Ocean in the area of the present-day NE Tibetan Plateau (Fig. 1a; Xiao et al., 2009; Yin et al., 2010; Gehrels et al., 2011; Fu et al., 2018; Yan et al., 2019a, b; Yu et al., 2019a, b; Dong et al., 2021). The belt consists of island arcs, ophiolites, oceanic islands, microcontinental blocks and early Paleozoic high-pressure and ultrahigh-pressure metamorphic belts (Gehrels et al., 2003; Xiao et al., 2009; Yin et al., 2010; Song et al., 2013, 2019; Zhang et al., 2013, 2017; Yan et al., 2015, 2019; Yu et al., 2017, 2019b, 2021; Fu et al., 2018, 2020; Zhang, 2020). Tectono-stratigraphically, the QOB can be subdivided into the North Qilian Belt, the Central Qilian Block and the South Qilian Belt (Fig. 1b).

2.1 North Qilian Belt (NQB)

The NQB is composed of early Paleozoic low-*T* eclogites, blueschists, ophiolites and island-arc volcanic rocks (Xiao et al., 2009; Song et al., 2013; Zhang et al., 2013, 2016, 2017), and it is widely accepted that it represents the product of subduction of the Proto-Tethyan oceanic plate (North Qilian oceanic plate) between the Alxa and Central

Qilian blocks (Xia et al., 2003, 2011). The NQB contains two discontinuously exposed, subparallel NW–SE-trending ophiolite belts that contain serpentinised peridotite, gabbro, basalt and dolerite dykes (Fig. 1b). Both ophiolite belts were reported as N-MORB and supra-subduction zone (SSZ) types, which indicates that bi-directional subduction occurred beneath the Central Qilian and Alxa blocks (*e.g.*, Wu et al., 2004; Fu et al., 2020; Yu et al., 2021).

HP/LT metamorphic rocks have been identified in the middle segment of the NQB, and three tectonic slices are recognised (Fig. 2a, b). These slices consist of various amounts of eclogite, blueschist, mica schist, metachert, marble and serpentinite. They run nearly parallel to each other, and they have similar rock associations and deformation, with metamorphic ages ranging from 490 to 460 Ma (Song et al., 2013, 2019; Zhang et al., 2017). Preliminary research has suggested that different types of NQB *HP/LT* metamorphic rock underwent different *P–T* evolution and peak metamorphic conditions, this being the case because of the complex fluxes of materials in the subduction channel (Wei et al., 2011; Zhang et al., 2017, 2021). The eclogites exposed mainly in the Baijingsi area to the east and in the Qingshuigou–Xiangzigou area to the west record peak metamorphic conditions of 2.1–2.6 GPa and 540–420 °C (*e.g.*, Zhang et al., 2021), and Yu et al. (2007) divided them into two subtypes based on their geochemistry. One type originated in an oceanic environment and the other type was derived from a continental/oceanic transitional zone or a continental margin. The blueschists in the NQB record peak *P–T* conditions of 1.9 GPa and 520 °C and a clockwise *P–T* path (Yu, 2017). This complex range of prograde, peak and retrograde

metamorphic conditions (Fig. 2a) reflects the complex fluxes of materials in the subduction channel of the Proto-Tethyan oceanic plate (North Qilian oceanic plate).

2.2 South Qilian Belt (SQB)

The SQB is located to the south of the CQB (Fig. 1b), and it consists mainly of the Neoproterozoic Hualong Complex, volcano-sedimentary rocks of Cambrian–Lower Ordovician age, sedimentary rocks of late Upper Ordovician–Silurian age and sedimentary rocks of Carboniferous–Triassic age (Xiao et al., 2009; Yan et al., 2015, 2019, 2021; Fu et al., 2018, 2020). The Cambrian volcano-sedimentary rocks are represented by a dismembered intra-oceanic subduction–accretionary system and a suite of Ordovician volcano-sedimentary rocks that formed in a subduction–collision related system (Song et al., 2013, 2017; Fu et al., 2018; Yan et al., 2019; Sun et al., 2020).

The Hualong Group is composed of granitic orthogneisses and psammitic paragneisses that represent the principal counterparts of the basement rocks of the CQB. The gneisses were modified by several geological processes during the subduction of the Proto-Tethyan oceanic plate (South Qilian oceanic plate), including the development of 470–440 Ma continental arc magmas, coeval arc-related regional metamorphism and anatexis. Integrated studies of whole-rock geochemistry, mineral assemblages, and geothermobarometry (biotite–garnet–plagioclase–quartz) reveal that these rocks probably originated from felsic–basic volcanic and sedimentary rocks that underwent 600–650 °C and 3.9–6.4 kbar amphibolite facies metamorphism (Fig. 1b; BGMR-GP, 1989; BGMR-QP, 1991; Yan et al., 2015). Li et al. (2018b) also reported garnet amphibolites in the Hualong Group that record

a clockwise *P*–*T* path with peak conditions of 4.9–6.3 kbar and 755–820 °C in the upper amphibolite facies and low-temperature granulite facies, followed by retrograde cooling and decompression at 2.5–3.1 kbar and 525–545 °C (dated at ca. 450 Ma), all of which took place during the northward subduction of the Proto-Tethyan oceanic plate (South Qilian oceanic plate).

2.3 Central Qilian Block (CQB)

The CQB is sandwiched between the NQB and the SQB and consists mainly of Precambrian metamorphic rocks that are overlain by upper Paleozoic shallow-marine sediments (Fig. 1b). The Precambrian rocks are distributed discontinuously in the Yemananshan, Huangyuan, and Maxianshan areas and were originally named the Tuolai, Huangyuan, and Maxianshan groups (BGMR-GP, 1989; BGMR-QP, 1991). They can be divided into two parts on the basis of metamorphic grade (Fig. 1c). The lower part consists of greenschist to amphibolite facies schists, migmatites, gneisses, Mg-enriched marbles, quartzites, amphibolites and metavolcanic rocks, with well-documented Neoproterozoic (940–788 Ma) granitoids and mafic intrusive rocks (Guo et al., 1999, 2000; Wan et al., 2003; Gehrels et al., 2003, 2011; Tung et al., 2013, 2016; Huang et al., 2015). The upper part consists of low-grade metavolcanic and metasedimentary rocks. The CQB therefore consists of middle Mesoproterozoic to Neoproterozoic rocks (Tung et al., 2013, 2016; Wu et al., 2017; Zuza, 2018). The tectonic affinity of the CQB has long been controversial. Some researchers have proposed that the CQB rifted from the North China Craton (*e.g.*, Feng, 1997, Xia et

al., 2003), and others have suggested that it was related to the South China Craton (Wan et al., 2000, 2003, 2006; Tung et al., 2013, 2016; Yan et al., 2015; Xu et al., 2016; Li et al., 2018a, 2020).

The Huangyuan Group, one of the major parts of the CQB, is distributed mainly in Huangyuan County, Huangzhong County and Ledu County of Qinghai Province (Fig. 1b). Geological mapping has revealed that the Huangyuan Group contains marble, metasilicic rocks, plagioclase amphibolites, amphibolites, quartzites, mica gneisses (schists) and granite gneisses, with the amphibolites and granite gneisses forming lenses or intrusions in the matrix of the Huangyuan Group (Fig. 3a). Geochemical data coupled with geological mapping indicate that the protoliths of these rocks were intermediate–basic volcano-sedimentary rocks deposited in an epicontinental back-arc basin (Guo et al., 1999, 2000; Wan et al., 2006; Tung et al., 2013). Interestingly, the metamorphic rocks of the Huangyuan Group record a more variable range of *P–T* conditions than do the rocks of the Maxianshan and Tuolai groups (Qi et al., 2004; Peng et al., 2017a, b; Li et al., 2018a, b, 2019; unpublished data). Moreover, the ca. 500 Ma *HT/LP* upper amphibolite- to granulite-facies metamorphism and the ca. 450 Ma *HT/MP* amphibolite facies metamorphism imply that the rocks of the Huangyuan Group record multiple episodes of overprinting metamorphism during the early Paleozoic (Peng et al., 2017a, b; Li et al., 2018b, 2019; unpublished data).

Our study area, the Datonghe area (Figs 1c and 3a), lies on the northern margin of the CQB (or southern margin of the NQB). Twenty-two samples from the Huangyuan Group, including felsic gneiss and amphibolite, were collected for analysis (Fig. 1c). The

amphibolites often occur as lenses in the adjacent gneiss or schist, and deformation features include small folds, *S–C* (*schistosité–cisaillement*) shear fabrics, rotated feldspar porphyroblasts and deformed boudins.

3 Analytical methods

U–Pb dating and trace element analyses of the zircons were undertaken via LA–ICP–MS at the School of Resources and Environmental Engineering, Hefei University of Technology, China. Standard zircon 91500 was used for external calibration, and ^{91}Zr as the internal standard. For trace elements, NIST610 was used as the external calibration standard and ^{29}Si as the internal standard. Details of the analytical methods used are given by Sun et al. (2020). For the U–Pb isotope analyses, ICPMSDataCal 7.0 (Liu et al., 2010) was used to calculate the zircon isotope ratios and trace elements. Common Pb was corrected as recommended by Anderson (2002). The analytical results are reported with 1σ error. The weighted mean U–Pb ages (90% confidence) were calculated at the 2σ level, and concordia plots were processed using Isoplot v. 3.23. The zircon U–Pb isotope compositions and trace element abundances determined using LA–ICP–MS are listed in Table 1.

Electron probe microanalysis (EPMA) was used to obtain the mineral compositions of gneiss sample 18WJF19 for thermobarometry. This analytical work was conducted at the School of Resources and Environmental Engineering, Hefei University of Technology (China), using a SHIMADZU JXA-8230 electron microprobe. The contents of the following oxides were determined: SiO_2, TiO_2, Al_2O_3,

Cr_2O_3, FeO, MnO, MgO, CaO, Na_2O and K_2O. The working conditions and analytical methods we used followed those described by Li et al. (2019b). The analytical results are summarised in Table 2.

Petrological modelling was performed for gneiss 18WJF19 in the $MnO–Na_2O–CaO–K_2O–FeO^{total}–MgO–Al_2O_3–SiO_2–H_2O–TiO_2–O_2$ (MnNCKFMASHTO) system using Perple_X 6.9.0 (Connolly, 2009; Connolly and Galvez, 2018). Whole-rock compositions were obtained for gneiss sample 18WJF19 using the P61-XRF26S X-ray fluorescence (XRF) spectrometer fusion method at the laboratory of ALS Chemex (Guangzhou) Co. Ltd., Guangzhou, China. Individual FeO and Fe_2O_3 contents for samples were determined via Fe-Vol05 titration, and the amount of aqueous fluid (H_2O) was determined by loss on ignition measurements. The bulk-rock compositions used for modelling (Table 3) were calculated by conversion of the whole-rock compositions (determined by ICP–MS) to model-ready bulk compositions (Palin et al., 2016). Gneiss sample 18WJF19 was modelled in the MNCKFMASHTO system using the following *a–x* relations: silicate melt, augite and hornblende (Green et al., 2016); garnet, orthopyroxene, biotite, muscovite and chlorite (White et al., 2014); olivine and epidote (Holland and Powell, 2011); cordierite (Holland and Powell, 1998) magnetite–spinel (White et al., 2002); ilmenite–hematite (White et al., 2000); and plagioclase–K-feldspar (Holland and Powell, 2003). Pure phases included rutile, andalusite, sillimanite, kyanite, quartz and aqueous fluid (H_2O).

The Raman spectra of kyanite inclusions in garnets were obtained using a laser Raman microspectrophotometer (LabRam HR Evolution; HORIBA JOBIN YVON) at

241 Hefei University of Technology (China). The 532-nm wavelength of a Modulaser
242 argon laser was used. The laser power on the sample surface was ~1–2 mW.
243
244 **4 Deformation of the Huangyuan Group**
245 **4.1 Macrostructures**
246 **Ductile Shear Belts:** There are four WNW–ESE-striking ductile shear belts in
247 the CQB, which have individual widths of tens of meters. Together, the four shear
248 belts form a band ~800 km long and 5–6 km wide (Qi et al., 2004; Xu et al., 2016).
249 The shear belts cut across metamorphic basement rocks of Precambrian age, and they
250 run parallel to the trend of the QOB. Detailed field observations showed that the
251 ductile shear belts are distributed from east to west in the Baiyin, Datonghe and
252 Tuolemuchang areas, and that they all possess similar structural characteristics. We
253 focused our research on the Datonghe area in the central part of the ductile shear belts
254 (Fig. 3a).
255 Protomylonites, mylonites and local ultramylonites are very common within the
256 shear belts (Fig. 3b–e), and the mylonitic foliations dip gently (<50°) to the SE,
257 probably reflecting the attitude of the whole shear belt (Fig. 3a). Mineral elongation
258 lineations, defined by elongate quartz and feldspar grains as well as orientated
259 hornblende or mica aggregates (Fig. 3c), trend between NW–SE and WNW–ESE.
260 Intra-folial folds with fold axes that plunge gently NW or SE, parallel to the mineral
261 elongation lineations, are common in the sheared metamorphic rocks. Sheared and
262 folded dykes have similar fold geometries. Undeformed dykes also occur in the

ductile shear belts, indicating post-shearing magmatic activity. Abundant *S–C* (*schistosité–cisaillement*) fabrics, rotated feldspar porphyroclasts, and asymmetric folds in the ductile shear belts all indicate dextral shear with minor reverse components (Fig. 3b–e). The change in attitude of the fabric with increasing proximity to the shear belts also demonstrates a dextral sense of shear.

Brittle Faults: Several brittle faults in the Datonghe area occur in a zone about 10 km wide, strike NW–SE and dip steeply (>60°; Fig. 4a, b). Striations on the fault planes plunge gently (generally <30°) to the NE or SW. Riedel shears and joints are often found adjacent to the strike-slip faults. NNW–SSE-striking faults parallel to the Riedel shears are also common between the strike-slip faults (Fig. 4b). A dextral shear sense is also supported by the orientations of striations, steps and drag folds.

4.2 Microstructures

To reach a better understanding of deformation in the ductile shear belts of the CQB, we collected oriented samples of mylonite. The oriented thin sections were cut parallel to the XZ plane of the finite strain, that is, perpendicular to foliation and parallel to the mineral lineation.

The widespread mylonitisation in the dextral ductile shear belts of the CQB produced protomylonites, mylonites and ultramylonites according to the increasing intensity of deformation, and the mylonitisation was characterised by dynamic recrystallisation of quartz (Figs 5 and 6a–f). Microscopic shear sense indicators such as *S–C* fabrics (Fig. 6f), rotated amphibole porphyroclasts (Fig. 6b), feldspar “bookshelf” structures (Fig. 6d) and

mica fish (Fig. 6c) indicate a dextral sense of shear (Fig. 6e–f). These kinematic characteristics observed in thin section are consistent with macrostructural evidence for right-lateral displacements.

The rims of garnet porphyroblasts, modified by late deformation involving quartz and sillimanite in the matrix, indicate a dextral sense of shear (Fig. 6a). Moreover, the quartz inclusions in garnet porphyroblasts are oblique to the surrounding foliation in the matrix (Fig. 6a, c), and this indicates that the garnet was formed earlier than the foliation. These features in the CQB are also consistent with the multi-stage metamorphism–deformation of the Huangyuan Group.

4.3 Estimates of the temperatures during deformation

We performed multi-disciplinary investigations to estimate the temperatures during deformation in the CQB. We focused mainly on the temperature of the late-stage deformation by examining dynamic recrystallisation mechanisms and quartz c-axis fabrics.

4.3.1 Dynamic recrystallisation

The styles of recrystallisation and deformation of quartz and feldspar are strongly temperature dependent (*e.g.*, Stipp et al., 2002; Mancktelow and Pennacchioni, 2004; Sato et al., 2019). In our mylonitised specimens, the widespread combination of bulging (BLG) and subgrain rotation (SR) recrystallisation of quartz indicates that shearing during mylonite formation took place at temperatures between

350 and 400 °C. BLG recrystallisation of quartz on its own suggests a temperature of 300–350 °C, whereas the local formation of subgrains in feldspar suggests temperatures of 400–450 °C (Stipp et al., 2002; Mancktelow and Pennacchioni, 2004; Passchier and Trouw, 2005; Wang et al., 2016). We used this information on the styles of recrystallisation in quartz to estimate the temperatures of deformation in the CQB ductile shear belts.

Mylonites in the Huangyuan Group show recrystallisation of both quartz and feldspar and/or elongation. Most mylonites show evidence of both SR and grain boundary migration (GBM) recrystallisation of quartz (Fig. 7a–d and Table 4) but some exhibit only SR recrystallisation of quartz. Most feldspars show fractures or elongation (Fig. 7a–d and Table 4), and in some mylonite samples we also observed bulging recrystallisation of feldspar. The styles of recrystallisation of quartz and feldspar are related to the temperature of deformation, and they can therefore be used as empirical geothermometers (Tullis and Yund, 1987; Stipp et al., 2002; Passchier and Trouw, 2005). In most of the samples of mylonite from the middle of the CQB, the styles of recrystallisation indicate deformation temperatures of 400–500 °C.

4.3.2 Quartz c-axis fabrics

Quartz c-axis fabrics can also be closely related to deformation temperatures (Tullis and Yund, 1987; Passchier and Trouw, 2005). We used a U-stage to analyse the quartz c-axis fabrics in eight oriented samples of mylonite from the ductile shear belts of the CQB. Stereographic projections of the measured quartz c-axes show monoclinic symmetry (Fig. 8a–h), indicating non-coaxial deformation (Passchier and Trouw, 2005). The asymmetry of

these c-axes with respect to the foliation (XY plane) indicates a dextral sense of shear within the ductile shear belts, which is consistent with field and microscopic observations.

The quartz c-axis plots for eight samples of mylonite (19ST12, 19ST03, 18ST09, 19ST18, 19WJF1, 18WJF19, 19WJF2 and 19WJF4) from the Datonghe area in the middle of the CQB show single centre girdles with near-periphery and central maxima (Fig. 8a–h). The near-periphery maxima are indicative of dominant intracrystalline slip along rhomb planes, whereas the central maximum is indicative of dominant slip along prism planes (Passchier and Trouw, 2005). The quartz c-axis patterns of the eight samples of mylonite suggest deformation temperatures of 400–500 °C. Given that these are the same temperatures that were indicated by dynamic recrystallisation, we conclude that the dextral ductile shearing developed under medium to low temperature conditions of 400–500 °C.

5 Petrography, mineralogy and geochronology

We collected samples of amphibolite (19ZN06) and gneiss (19ZN39 and 18WJF19) for further research on the petrography, mineral chemistry, metamorphic ages and *P*–*T* conditions of rocks in the Datonghe area (Fig. 1b). The mineral abbreviations used are from Whitney and Evans (2010). The amphibolites in this area are surrounded by or intrude the paragneiss and orthogneiss country rocks. In the field, many small felsic leucosomes can be observed within the gneisses and amphibolites,

and these leucosomes characteristically form thin layers, veinlets or irregular masses (Fig. 9a).

5.1 Petrography

Amphibolite 19ZN06 consists mainly of garnet (15%), hornblende (60%), biotite (10%) and quartz (15%; Fig. 9b). The garnet porphyroblasts are subhedral with diameters ranging from 1.0 to 1.5 mm (Fig. 9b). Occasional retrogressed and sericitised plagioclase crystals in the matrix have lengths ranging from 1.0 to 2.0 mm. Hornblende crystals in the matrix have lengths of 1.0–2.0 mm and contain inclusions of plagioclase, quartz and ilmenite.

Gneiss 19ZN39 consists mainly of garnet (10%), biotite (10%), plagioclase (40%) and quartz (40%; Fig. 9c). The garnet porphyroblasts are euhedral to subhedral, with diameters ranging from 1.0 to 2.0 mm (Fig. 9c).

Gneiss 18WJF19 contains plagioclase (27%), quartz (45%), biotite (15%), garnet (8%) and sillimanite (5%) as well as minor chlorite, titanite and ilmenite (Fig. 9d). Euhedral garnet grains are 1.5–3 mm in size and their cores contain inclusions of biotite, plagioclase, kyanite and quartz whereas their rims have no inclusions. The biotite in the matrix occurs as small relict grains. Sillimanite occurs mostly as large prismatic needles that define the matrix foliation and are commonly associated spatially with biotite. Plagioclase occurs throughout the matrix. Some large biotite grains in the matrix are replaced by ilmenite. The peak metamorphic mineral assemblage is interpreted to be Grt + Bt + Ilm + Sil + Pl + Qz ± H_2O.

372

373 **5.2 Mineral chemistry**

374 We used an electron probe microanalyser (EPMA) to obtain the representative
375 compositions of minerals in sample 18WJF19, which were then used for
376 thermobarometry (Fig. 10a–d). The Fe_2O_3 contents of minerals were calculated by
377 stoichiometry (Droop, 1987; Powell et al., 2014).

378 Our analyses show that garnet porphyroblasts in 18WJF19 (Fig. 9a) have high
379 almandine [$Fe^{2+}/(Fe^{2+} + Mg + Ca + Mn)$] and pyrope [$Mg/(Fe^{2+} + Mg + Ca + Mn)$]
380 contents (X_{Alm} = 0.63–0.59; X_{Pry} = 0.38–0.34) but low grossular [$Ca/(Fe^{2+} + Mg + Ca$
381 $+ Mn)$] and spessartine [$Mn/(Fe^{2+} + Mg + Ca + Mn)$] contents ($X_{Grs}$ = 0.03–0.02; X_{Sps}
382 = 0.01; Fig. 10b). From cores to rims, the garnet porphyroblasts show increases in
383 almandine content, but gradual decreases in pyrope content (Fig. 10b), and this
384 indicates that the garnets have been modified at their rims by retrograde
385 metamorphism.

386 The plagioclase in gneiss 18WJF19 is dominantly oligoclase (Fig. 10d), with
387 X_{An} [Ca/(Ca + Na)] = 0.30 and X_{Ab} [Na/(Na + Ca + K)] = 0.70. The plagioclase is
388 relatively homogeneous.

389

390 **5.3 U–Pb zircon geochronology**

391 To determine the age of the metamorphism in the CQB, three samples were
392 collected for zircon U–Pb age dating. Sample locations are shown on Fig. 1c.
393 Amphibolite sample 19ZN06 and gneiss sample 19ZN39 were collected from a

394 weakly deformed area, and gneiss 18WJF19 was collected from a ductile shear zone that
395 exhibits strong deformation.

396 **19ZN06:** two types of zircons were identified in this amphibolite. In
397 cathodoluminescence (CL) images, the type I zircons are mostly tabular and bright with
398 weak planar zoning, or round and subhedral (Fig. 11a). These zircons are relatively large
399 with lengths ranging from 150 to 250 μm. The type II zircons are smaller subhedral grains
400 of 100–250 μm long that exhibit core–rim textures. The rims, characterised by wide, weak,
401 oscillatory or patchy zoning, surround oscillatory-zoned low luminescent cores (Fig. 11a).
402 Analyses were conducted on 12 spots on Type I zircons and Type II zircon rims. Nine
403 analyses with concordia ages yielded weighted mean $^{206}Pb/^{238}U$ ages of 452 ± 6 Ma
404 (MSWD = 0.28; Fig. 11a) and low Th/U ratios of 0.11–0.48. Analyses were also conducted
405 on 11 spots on Type II zircon cores, and these inherited cores with high Th/U ratios of
406 0.32–1.16 yield various ages ranging from 1145 to 503 Ma. Based on the zircon
407 microtextures and low Th/U ratios of the Type I zircons and Type II zircon rims, we
408 propose that the age of metamorphism was *ca.* 452 Ma.

409 **19ZN39:** the zircons in gneiss 19ZN39 are mostly long or prismatic in shape, and
410 they have lengths of 100–200 μm with length/width ratios of 1.2–2.0. As shown in the CL
411 images, most grains display complicated core–rim textures, and some zircons show wide
412 oscillatory zones, which indicates a magmatic origin (*e.g.*, Hoskin and Schaltegger, 2003).
413 The cores and rims of the zircons from sample 19ZN39 produced variable analytical data.
414 The inherited cores of the zircons are characterised by Th/U ratios that range from 0.36 to
415 1.23 and $^{206}Pb/^{238}U$ ages of 510–481 Ma that yield a weighted mean $^{206}Pb/^{238}U$ age of 501 ±

11 Ma (n = 6, MSWD = 0.22; Fig. 11b), implying the existence of magmatic activity at ca. 500 Ma in the region. The rims of the zircons have Th/U ratios that range from 0.06 to 0.79 and $^{206}Pb/^{238}U$ ages of 466–420 Ma that yield a weighted mean $^{206}Pb/^{238}U$ age of 449 ± 8 Ma (n = 10, MSWD = 0.81; Fig. 11b), which we interpret to be the metamorphic age of orthogneiss 19ZN39.

18WJF19: the zircons from gneiss 18WJF19 are mostly long or prismatic in shape, and they have lengths of 100–250 μm with length/width ratios of 1.2–2.0 (Fig. 11c). As shown in the CL images, most zircons in sample 18WJF19 possess narrow rims that are too thin to be dated (Fig. 11c). Three large-enough rims gave $^{206}Pb/^{238}U$ ages of 457, 455, and 447 Ma, indicating a metamorphic event in the Late Ordovician, which is consistent with the Late Ordovician metamorphism recorded by samples 19ZN06 and 19ZN39. The cores of the zircons from gneiss sample 18WJF19 gave ages ranging from 1661 to 1596 Ma, which might represent the ages of the protolith (Table 2).

6 Petrological modelling

Petrological modelling is a highly effective method of assessing the thermal evolution of metamorphic rocks (White et al., 2004; Diener et al., 2008), and it can constrain prograde, peak and/or retrograde *P–T* conditions with much better precision than conventional thermobarometry (Palin et al., 2016; Forshaw et al., 2019). We applied this modelling to gneiss sample 18WJF19 (Fig. 12a–b).

A bulk-rock pseudosection calculated for sample 18WJF19 under *P*–*T* conditions of 5.5–10 kbar and 550–850 °C is shown in Fig. 12a. The observed mineral assemblage of Grt–Bt–Pl–Ilm–Sil–Qtz is stable over a broad range of *P*–*T* conditions at >6 kbar and >700 °C (Fig. 12a). The low-temperature limit of this calculated assemblage field is defined by the kyanite–sillimanite polymorphic transition. At the low-pressure limit, cordierite becomes stable, and since this mineral is not observed in sample 18WJF19, a minimum peak pressure of 5.5–6 kbar at 700–800 °C is indicated. Independent estimates of peak metamorphism obtained with the GBPQ geothermometer (6.3–7.7 kbar and 703–762 °C; unpublished data; Wu et al., 2004) show a degree of overlap with the peak assemblage field defined on this calculated pseudosection, which indicates that the final chemical equilibrium prior to solidification of the incipient partial melt occurred at around 7–7.5 kbar and 700–750 °C.

The garnet in 18WJF19 preserves growth zoning, with a preserved peak metamorphic composition in the core and a retrograde metamorphic composition in the rim (Fig. 9b). The calculated garnet core and plagioclase composition isopleths for sample 18WJF19 are shown in Fig. 10a, and we used isopleths of X_{Mg} = [Mg / (Fe^{2+} + Ca + Mg + Mn)] and X_{Ca} = [Ca / (Fe^{2+} + Ca + Mg + Mn)] for garnet and X_{Ca} = [Ca / (Ca + Na)] for plagioclase as three independent thermodynamic variables to constrain the peak metamorphic conditions more accurately. X_{Mg} in the garnet cores increases with increasing temperature and X_{Ca} in the garnet cores increases with increasing pressure (Fig. 12a). Isopleths of X_{Ca} for plagioclase have moderately negative slopes that increase as pressure rises (Fig. 12a). The isopleths of X_{Mg} = 0.38 and X_{Ca} = 0.03 (Table 3) that represent the garnet mantle and the isopleth of X_{Ca}

= 0.3 for plagioclase intersect at the upper stability limit of the observed early mineral assemblage, indicating peak metamorphic *P–T* conditions of ~740 °C and ~7.2 kbar (red circle on Fig. 12a) for paragneiss 18WJF19, equivalent to conditions of the medium-pressure/high-temperature (*MP/HT*) upper amphibolite facies. This predicted assemblage also contains minor amounts of a silicate melt, which is consistent with observations of incipient anatexis in outcrops of the paragneiss (Fig. 9).

Representative compositional isopleths for the garnet rims were used to estimate the conditions of the retrograde metamorphism. The isopleths of X_{Mg} = 0.35 and X_{Ca} = 0.02 for garnet rims intersect at *P–T* conditions of ~670 °C and ~5.5 kbar (blue circle on Fig. 12a), indicating a peak-to-retrograde *P–T* path that involved cooling and minor decompression (Fig. 12b). The retrograde *P–T* path systematically crosses isopleths of free H_2O content, which indicates that the melt preserved in the rocks started to crystallise and react with the residual, thus representing the reverse reaction of the partial melting that occurred during uplift. The modelling shows that after the peak metamorphism the rocks of the Huangyuan Group underwent cooling and decompression.

7 Discussion

7.1 Timing of metamorphism

Constraints on the timing of metamorphism and deformation in the CQB could provide important constraints on the evolution of the Proto-Tethys Ocean. In this regard, three groups of ages were obtained for samples 18WJF19, 19ZN06, and

19ZN39. Group 1 (465–441 Ma) ages were obtained from zircon rims (18WJF19, 19ZN06 and 19ZN39). Group 2 (*ca.* 500 Ma) ages were obtained from the cores of the 19ZN39 zircons. Group 3 (1661–1040 Ma) ages were obtained from inherited zircon cores. The 465–441 Ma group 1 zircons possess low Th/U ratios and show grey luminescence and planar zoning in CL images, which suggests these zircons are metamorphic and that they crystallised during the Late Ordovician. The *ca.* 500 Ma group 2 zircons have typical magmatic characteristics with oscillatory zoning and high Th/U ratios, and they record an episode of magmatism. In fact, numerous examples of 500 Ma magmatic and500 Macoeval c metamorphic rocks have been reported in the CQB (*e.g.,* Tung et al., 2013; Peng et al., 2017a, b; Li et al., 2019b; Fu et al., 2020; Yu et al., 2021), indicating that the CQB underwent extensive magmatic–metamorphic modifications during the early Paleozoic. The inherited group 3 zirconszircons occur mainly as zircon cores, and they probably reflect the ages of the protoliths.

^{40}Ar–^{39}Ar dating is commonly used to constrain a cooling or crystallisation age after a high-temperature event. In the central part of the ductile shear belt, biotites from different lithologies have yielded $^{40}Ar/^{39}Ar$ ages of 422 to 380 Ma, and these ages span more than 40 Myr (*e.g.,* Qi et al., 2004; Li et al., 2018c). We have shown above that the deformation occurred at temperatures of 400–500 °C, and this means that the biotite ages are cooling ages, and that the ductile shear belt formed before 420 Ma. Petrographic observations have shown that inclusions (such as quartz) in the garnet porphyroblasts have different orientations from the grains in the matrix. Moreover, we know that the rims of the garnets were modified by ductile shearing (Fig. 5a, e). These observations indicate that the ductile

shearing took place after the garnets were formed during the period 452–445 Ma. Moreover, in the eastern part of the ductile shear zone (the Baiyin area), undeformed magmatic plutons with emplacement ages of 402–388 Ma (LA–ICP–MS U–Pb zircon age dating) are present in the ductile shear belt (Yin, 1998; Guo, 2001). In contrast, 468–440 Ma (LA–ICP–MS U–Pb zircon age dating) intrusive rocks (quartz–albite porphyries) are deformed, indicating that the ductile shearing took place during the period 440–425 Ma. Furthermore, Carboniferous strata overlie the ductile shear belt in the eastern part of the CQB (Qi et al., 2004). Considering the zircon ages we obtained, and remembering that different minerals have different closure temperatures, we suggest that the ductile shear-zone deformation probably took place during the Silurian (440–420 Ma).

7.2 *P–T* path and multi-stage metamorphism

Constraints on the prograde metamorphic *P–T* evolution can be provided by the mineral inclusions in garnet cores. Kyanite inclusions were identified by Raman intensity mapping of the garnet cores (Fig. 10e, f). The *P–T* path we propose was a clockwise loop, based on the visible inclusions of biotite, plagioclase, kyanite and quartz (Fig. 12b) being stable at lower temperatures and pressures. The *P–T* paths of metamorphic rocks provide important information on the evolution of an orogen and the associated tectonic processes (*e.g.*, Thompson and Ridley, 1987; Brown, 1993; Lee and Cho, 2003). The Huangyuan ca. 450 Ma *HT–MP* metamorphic rocks record a typical clockwise *P–T* path, which involved the deep burial of crustal rocks and subsequent thermal relaxation, followed by

quasi-isobaric cooling. This type of *P–T* path is typical of continental crust that has been doubled in thickness by collision (Thompson and England, 1984; Thompson and Ridley, 1987; Brown, 1993; Wei et al., 1998), and collisional thickening could reasonably account for the formation of the Huangyuan *HT–MP* metamorphic rocks. Numerous 455–430 Ma syn-collisional magmatic rocks are distributed in the Leigongshan, Wuqiaoling and Niuxinshan areas of the NQB and CQB, and these magmatic rocks have high values of Sr/Y and $(La/Yb)_N$, low values of $Mg^{\#}$, low contents of Cr and Ni, and negative $\varepsilon_{Nd(t)}$ values (Tseng et al., 2009; Wu et al., 2010, 2011; Song et al., 2013; Huang et al., 2015; Chen et al., 2016, 2018). Moreover, the youngest ophiolite emplacement age recorded the NQB is ca. 450 Ma (in the Laohushan area; Fig. 1b; *e.g.*, Song et al., 2013; Zhang et al., 2017), and the youngest Ar–Ar plateau ages of NQB phengites are 446–454 Ma (Liou et al., 1989; Liu et al., 2006; Yu et al., 2021). These data indicate that the *HT–MP* metamorphic rocks in our study area were formed during the continental collision of the CQB and the Alxa Block. Therefore, the absolute peak *P–T* conditions and the proposed burial path of paragneiss 18WJF19 are consistent with a geodynamic setting of continental collision (*e.g.*, Liou et al., 2004; Burg and Gerya, 2005).

Our microstructural analyses and petrographic and thermobarometric datasets indicate that the Huangyuan Group records at least two stages of deformation–metamorphism: early upper amphibolite facies metamorphism (M_1), and a later stage of low-grade dextral ductile shearing (M_2).

Low-temperature mineral assemblages and macro- and micro-structures indicating plastic deformation are found in the mylonitic rocks of the CQB. The mylonites have

mineral stretching lineations with typical L- and S–L-type fabrics. Feldspar, hornblende and quartz exhibit evidence of dynamic recrystallisation, whereas fine-grained, elongate, oriented feldspar, polycrystalline ribbons of quartz and fine-grained mica (Figs 3 and 5–7) record low-temperature plastic deformation (Passchier and Trouw, 2005). The dynamic recrystallisation and quartz c-axis fabrics of the Huangyuan Group indicate that the low-temperature deformation (M_2) took place at temperatures of 400–500 °C. In the field, nearly horizontal mineral elongation lineations within the XY foliation planes are well developed in the dextral strike-slip ductile shear zones, and they indicate a non-coaxial plane strain regime that is consistent with the strain indicated by the quartz c-axis fabrics. In the YZ plane, perpendicular to foliation and lineation, symmetrical speckles or boudins with long axes parallel to the Y axis are developed without evidence of rotation, indicating simple shearing. All these structural features indicate that large-scale dextral strike-slip movements occurred along the northern margin of the CQB in a tectonic setting of oblique collision during the period 440–420 Ma.

In contrast, the petrological modelling for sample 18WJF19 suggests that this region underwent *HT–MP* metamorphism with peak temperature conditions of ~740 °C, much higher than the temperatures of M_2. Petrographical observations show that the rims of garnet porphyroblasts have been modified, with evidence for the same sense of rotation as indicated by the minerals in the matrix, and the mica foliations exhibit two different orientations, which could further support the idea of multi-stage metamorphism–deformation (Fig. 7a, e). Moreover, the results of zircon age dating and ^{40}Ar–^{39}Ar dating also confirm that M_1 took place before M_2. Our data show, therefore, that

569 the rocks of the Huangyuan Group record two stages of metamorphism–deformation (M_1
570 and M_2) during the early Paleozoic.

571 Peng et al. (2017a) obtained zircon U–Pb dates of 498.9 ± 4.1, 504.4.3 ± 3.9, and
572 499.3 ± 2.9 Ma for the metamorphism in the Huangyuan Group. The 504 Ma Grt–Bt gneiss
573 (Grt, Bt, Ms, Pl, Kf, Sill, Ilm and Qz) records peak *P–T* conditions of ~720 °C and ~6.4
574 kbar, and the 498 Ma garnet amphibolite (Grt, Pl, Amp, Ilm and Qz) records conditions of
575 ~700 °C and ~7.1 kbar, which together define an anticlockwise *P–T* path. The peak
576 conditions and *P–T* path that indicate upper amphibolite to granulite facies metamorphism
577 in the early Paleozoic could have been related to the coeval magmatism that developed
578 during the subduction of the North Qilian oceanic plate (Bohlen, 1991; Zhao and Zhai,
579 2013; Peng et al., 2017a). Furthermore, the Group 2 magmatic zircon core ages we obtained
580 (*ca.* 500 Ma) are consistent with reports of widespread 500 Ma metamorphic and magmatic
581 activity in the CQB (Peng et al., 2017b; Zhang et al., 2017; Dong et al., 2021; Yu et al.,
582 2021). Tying all these data and observations together lead us to propose that at least three
583 stages of metamorphism are recorded in the Huangyuan Group of the CQB: initial
584 high-temperature/low-pressure metamorphism (M_0) under granulite-facies conditions at *ca.*
585 500 Ma, subsequent metamorphism under upper amphibolite-facies conditions (M_1) at *ca.*
586 450 Ma and a later stage of low-grade metamorphism (M_2) and dextral ductile shearing at
587 440–420 Ma.

588

589 **7.3 Tectonic implications**

590 The North Qilian Ocean was one of the branches of the Proto-Tethys Ocean, and
591 much of the research into this branch has been focused on subduction polarity during the
592 early Paleozoic. Many models have been proposed to explain the processes associated
593 with the closure of the North Qilian Ocean, including southward subduction (Liu et
594 al., 2005; Gehrels et al., 2011), northward subduction (Xu et al., 1994; Xia et al.,
595 2016), double subduction (Wu et al., 2011; Zhang et al., 2015; Yu et al., 2021), and
596 multiple-accretionary processes (Yan et al., 2007, 2010, 2021; Xiao et al., 2009; Fu et
597 al., 2020). Unfortunately, the uncertainty about the polarity of subduction and timing
598 of closure of the ocean (*e.g.,* Xiao et al., 2009; Song et al., 2013, 2019; Li et al., 2018;
599 Fu et al., 2020; Yan et al., 2021) restricts our understanding of the evolution of the
600 Proto-Tethys Ocean.

601 The three stages of metamorphism (M_0, M_1 and M_2) we propose in this paper
602 can be related to subduction and closure of the Proto-Tethys Ocean. The *ca.* 500 Ma
603 *LP/HT* metamorphism (M_0) in the CQB was granulite facies metamorphism that took
604 place in an elevated geothermal gradient of more than 75 °C/kbar (Peng et al., 2017a,
605 b), which is characteristic of metamorphism in an arc that overlies an orogenic system.
606 In contrast, the *ca.* 500 Ma *HP/LT* metamorphism in the NQB was eclogite facies
607 metamorphism that took place in a relatively cold geothermal gradient of less than
608 35 °C/kbar (Wei and Song, 2008; Zhang et al., 2013, 2017; Zhang, 2020), which is
609 characteristic of metamorphism in a subducted slab (Palin et al., 2016b). These two
610 different thermal gradients could be regarded as being consistent with the model of

paired metamorphic belts (Miyashiro, 1961, 1973; Brown, 1993, 2009, 2010), which would provide further support for the southward subduction of the North Qilian oceanic plate. In such a case, therefore, M_0 would have been related to subduction of the Proto-Tethyan oceanic plate.

The rocks metamorphosed during M_1 at *ca.* 450 Ma record a clockwise *P–T* path with *MP/HT* peak *P–T* conditions, and this metamorphism could be related to continental collision with M_1 developing on the hanging wall. The rocks metamorphosed during M_2 at 440–420 Ma were formed in relation to oblique collision during closure of the North Qilian Ocean, and they are consistent with southward subduction. Meanwhile, the Cambrian ophiolite complexes of the NQB and the numerous Early–Middle Ordovician igneous rocks that were intruded into the northern margin of the CQB also indicate south-dipping subduction of the North Qilian oceanic plate beneath the CQB (Tseng et al., 2009; Wu et al., 2009; Peng et al., 2017a, b). Thus, there is much evidence to support the existence of southward subduction of the North Qilian oceanic plate during the early Paleozoic and the connection between the M_1 and M_2 metamorphic events and the closure of the Proto-Tethys Ocean. The timing of closure of the North Qilian Ocean can be traced from the minimum metamorphic age of the *HP/LT* metamorphism and the timing of the latest arc magmatism and SSZ-type ophiolite. This means that the closure of the North Qilian Ocean and the initial collision probably took place in the Late Ordovician, as evidenced by: (1) the youngest ophiolites (Laohushan area, ca. 450 Ma, Fig. 1b; *e.g.*, Song et al., 2013; Zhang et al., 2013, 2017; Zhang, 2020); (2) syn-collisional magmatism (460–450 Ma; Wu et al., 2010, 2011; Song et al., 2013; Huang et al., 2015; Chen et al., 2016, 2018); (3) arc-related

volcanic rocks, consisting of MORB-like forearc basalts and mafic–felsic volcanic rocks that formed between 517 and 445 Ma (Zhang and Xu, 1995; Zhang et al., 1997; Wang et al., 2005; Fu et al., 2020); (4) the youngest Ar–Ar plateau ages of phengite from subduction-related high-grade blueschists (454–446 Ma; Liou et al., 1989; Liu et al., 2006); and (5) the M_1 and M_2 metamorphic events. Moreover, the Middle–Late Ordovician detrital zircon ages and geochemistry suggest that the provenance of the Tianzhu Group in the eastern part of the NQB changed from arc-related rocks in the Middle Ordovician to sediments from the Alxa Block and the CQB in the Late Ordovician, indicating a transformation of sedimentary facies from marine to terrestrial during the Late Ordovician (Xu et al., 2010a, b).

8 Conclusions

We used zircon U–Pb ages, mineral chemical analyses, phase equilibrium modelling, evidence of dynamic recrystallisation and quartz c-axis fabric analyses to constrain the timing and *P–T* conditions of metamorphism and deformation of Huangyuan Group rocks in the CQB of the Tibetan Plateau. Our major conclusions are as follows.

1. LA–ICP–MS U–Pb ages of zircons from three CQB samples show that the peak metamorphic event took place between 452 and 445 Ma. Based on field relationships and reconsiderations of earlier reported isotopic dating, we show that the dextral ductile shear belt along the northern margin of the CQB is Silurian in age (440–420 Ma), and obviously younger than the peak metamorphism.

2. We identified two stages of metamorphism and deformation. Phase equilibrium modelling suggests that the region underwent *HT–MP* metamorphism (M_1) involving a clockwise *P–T* path, peak conditions of ~740 °C and ~7.2 kbar, and subsequent retrogression at ~670 °C and ~5.5 kbar. The second stage of metamorphism (M_2) involved dextral ductile shear deformation at medium to low temperatures (400–500 °C) that is recorded in mylonitic rocks with evidence of dynamic recrystallisation and southward production of monoclinic quartz c-axis fabrics.

3. High-grade metamorphism at *ca.* 450 Ma and the ductile shear deformation at 440–420 Ma in the CQB provide evidence for southward subduction during the closure of the North Qilian Ocean.

Acknowledgements

We sincerely commemorate Prof. Jiliang Li, who made great contributions to the development of Chinese tectonics. We also thank Dr. Quanzhong Li for LA-ICPMS analyses, Dr. Juan Wang for Electron Probe Micro Analysis, Dr. Yuefeng Shen for the polish of language and Dr. Qi Wu for the discussion. We are grateful to Prof. Michel Faure and two anonymous reviewers whose critical comments and constructive evaluation have significantly improved the quality of the paper. This study was supported by the National Natural Science Foundation of China (41272221, 41772228, 41902235).

Declaration of competing interest

The authors declare that they have no known competing financial interests or personal relationships that could have appeared to influence the work reported in this paper.

Credit authorship contribution statement

Yi Sun: Formal analysis, investigation, and writing-original draft. Manlan Niu: Supervision, funding acquisition, and writing-review. Zhen Yan: Writing-review & editing, investigation. Richard M. Palin: Writing-review and editing. Chen Li: Investigation and review. Xiucai Li: Investigation & review. Xiaoyu Yuan: Investigation.

References

Andersen, T., 2002. Correction of common lead in U-Pb analyses that do not report 204Pb. Chemical Geology 192, 59–79. https://doi.org/10.1016/S0009-2541(02)00195-X

BGMR-GP (Bureau of Geology and Mineral Resources of Gansu Province), 1989. Regional Geology of Qinghai Province. Geological Publishing House, Beijing (in Chinese).

BGMR-QP (Bureau of Geology and Mineral Resources of Qinghai Province), 1991. Regional Geology of Qinghai Province. Geological Publishing House, Beijing (in Chinese).

Brown, Michael, 1993. P-T-t evolution of orogenic belts and the causes of regional metamorphism. Journal of the Geological Society 16, 67–81. https://doi.org/10.1144/GSL.MEM.1995.016.01.09

Brown, M., 2010. Paired metamorphic belts revisited. Gondwana Research 18, 46–59. https://doi.org/10.1016/j.gr.2009.11.004

Brown, M., Johnson, T., 2019. Metamorphism and the evolution of subduction on Earth. American Mineralogist 104, 1065–1082. https://doi.org/10.2138/am-2019-6956

Burg, J.P., Gerya, T. v, 2005. The role of viscous heating in Barrovian metamorphism of collisional orogens: thermomechanical models and application to the Lepontine Dome in the Central Alps. Journal of Metamorphic Geology 23, 75–95. https://doi.org/10.1111/j.1525-1314.2005.00563.x

Cao, H., Cong, Y., Li, G., Xu, C., Vervoort, J., Kylander-Clark, A., 2015. Constrain multistage deformation using garnet Lu-Hf and monazite U-Pb dating: A case study of Tuolemuchang, North Qilian. Acta Petrologica Sinica 31, 3755–3768.

Cawood, P.A., Korsch, R.J., 2008. Assembling Australia: Proterozoic building of a continent. Precambrian Research 166, 1–38. https://doi.org/10.1016/j.precamres.2008.08.006

Cawood, P.A., Nemchin, A.A., Strachan, R., Prave, T., Krabbendam, M., 2007. Sedimentary basin and detrital zircon record along East Laurentia and Baltica during assembly and breakup of Rodinia. Journal of the Geological Society 164, 257–275. https://doi.org/10.1144/0016-76492006-115

Chen, S., Niu, Y., Li, J., Sun, W., Zhang, Y., Hu, Y., Shao, F., 2016. Syn-collisional adakitic granodiorites formed by fractional crystallization: Insights from their enclosed mafic magmatic enclaves (MMEs) in the Qumushan pluton, North Qilian Orogen at the northern margin of the Tibetan Plateau. Lithos 248, 455–468. https://doi.org/10.1016/j.lithos.2016.01.033

718 Chen, S., Niu, Y., Xue, Q., 2018. Syn-collisional felsic magmatism and continental crust
719 growth: A case study from the North Qilian Orogenic Belt at the northern margin of the
720 Tibetan Plateau. Lithos 308, 53–64. https://doi.org/10.1016/j.lithos.2018.03.001
721 Connolly, J.A.D., 2009. The geodynamic equation of state: What and how. Geochemistry
722 Geophysics Geosystems 10. https://doi.org/10.1029/2009gc002540
723 Connolly, J.A.D., Galvez, M.E., 2018. Electrolytic fluid speciation by Gibbs energy
724 minimization and implications for subduction zone mass transfer. Earth and Planetary
725 Science Letters 501, 90–102. https://doi.org/10.1016/j.epsl.2018.08.024
726 Dong, Y., Sun, S., Santosh, M., Zhao, J., Sun, J., He, D., Shi, X., Hui, B., Cheng, C., Zhang,
727 G., 2021. Central China Orogenic Belt and amalgamation of East Asian continents.
728 Gondwana Research. https://doi.org/10.1016/j.gr.2021.03.006
729 Dunlap, W.J., 1997. Neocrystallization or cooling? 40Ar/39Ar ages of white micas from
730 low-grade mylonites. Chemical Geology 143, 181–203.
731 https://doi.org/10.1016/S0009-2541(97)00113-7
732 Dunlap, W.J., Teyssier, C., McDougall, I., Baldwin, S., 1991. Ages of deformation from K/Ar
733 and 40 Ar/ 39 Ar dating of white micas. Geology 19, 1213–1216.
734 https://doi.org/10.1130/0091-7613(1991)019<1213:AODFKA>2.3.CO
735 England, P.C., Thompson, A.B., 1984. Pressure - temperature - time paths of regional
736 metamorphism I. heat transfer during the evolution of regions of thickened continental
737 crust. Journal of Petrology 25, 894–928. https://doi.org/10.1093/petrology/25.4.894
738 Feng, Y., 1997. Investigatory summary of the Qilian orogenic belt, China: history, presence
739 and prospect. Advance in Earth Science 12, 307–314.

740 Forshaw, J.B., Waters, D.J., Pattison, D.R.M., Palin, R.M., Gopon, P., 2019. A comparison of
741 observed and thermodynamically predicted phase equilibria and mineral compositions
742 in mafic granulites. Journal of Metamorphic Geology 37, 153–179.
743 https://doi.org/10.1111/jmg.12454
744 Fu, C., Yan, Z., Aitchison, J.C., Xiao, W., Buckman, S., Wang, B., Li, W., Li, Y., Ren, H.,
745 2020. Multiple subduction processes of the Proto-Tethyan Ocean: Implication from
746 Cambrian intrusions along the North Qilian suture zone. Gondwana Research 87,
747 207–223. https://doi.org/10.1016/j.gr.2020.06.007
748 Fu, C., Yan, Z., Wang, Z., Buckman, S., Aitchison, J.C., Niu, M., Cao, B., Guo, X., Li, X., Li,
749 Y., Li, J., 2018. Lajishankou Ophiolite Complex: Implications for Paleozoic Multiple
750 Accretionary and Collisional Events in the South Qilian Belt. Tectonics 37, 1321–1346.
751 https://doi.org/10.1029/2017tc004740
752 Gehrels, G., Kapp, P., DeCelles, P., Pullen, A., Blakey, R., Weislogel, A., Ding, L., Guynn, J.,
753 Martin, A., McQuarrie, N., Yin, A., 2011. Detrital zircon geochronology of pre-Tertiary
754 strata in the Tibetan-Himalayan orogen. Tectonics 30.
755 https://doi.org/10.1029/2011tc002868
756 Gehrels, G.E., Yin, A., Wang, X.F., 2003. Magmatic history of the northeastern Tibetan
757 Plateau. Journal of Geophysical Research-Solid Earth 108.
758 https://doi.org/10.1029/2002jb001876
759 Green, E.C.R., White, R.W., Diener, J.F.A., Powell, R., Holland, T.J.B., Palin, R.M., 2016.
760 Activity–composition relations for the calculation of partial melting equilibria in

761 metabasic rocks. Journal of Metamorphic Geology 34, 845–869.
762 https://doi.org/10.1111/jmg.12211
763 Guo, J., Zhao, F., Li, H., 1999. Jinningian collisional granite belt in the eastern sector of the
764 Central Qilian Massif and its implication. Acta Geoscientica Sinica (Diqiu Xuebao) 20,
765 10–15 (in Chinese with English abstract).
766 Guo, J., Zhao, F., Li, H., Li, H., Zuo, Y.C., 2000. New chronological evidence of the age of
767 Huangyuan Group in the eastern segment of Mid-Qilian massif and its geological
768 significance. Regional Geology of China 19, 26–31 (in Chinese with English abstract).
769 Hoffman, P.F., 1991. Did the breakout of Laurentia turn Gondwanaland inside-out? Science
770 252, 1409–1412. https://doi.org/10.1126/science.252.5011.1409
771 Holland, T.J.B., Powell, R., 2011. An improved and extended internally consistent
772 thermodynamic dataset for phases of petrological interest, involving a new equation of
773 state for solids. Journal of Metamorphic Geology 29, 333–383.
774 https://doi.org/10.1111/j.1525-1314.2010.00923.x
775 Holland, T., Powell, R., 2003. Activity-compositions relations for phases in petrological
776 calculations: An asymetric multicomponent formulation. Contributions to Mineralogy
777 and Petrology 145, 492–501. https://doi.org/10.1007/s00410-003-0464-z
778 Holland, T.J.B., Powell, R., 1998. An internally consistent thermodynamic data set for phases
779 of petrological interest. Journal of Metamorphic Geology 16, 309–343.
780 https://doi.org/10.1111/j.1525-1314.1998.00140.x
781 Hoskin, P.W.O., Schaltegger, U., 2003. The composition of zircon and igneous and
782 metamorphic petrogenesis. Zircon 53, 27–62. https://doi.org/10.2113/0530027

783 Huang, H., Niu, Y.L., Nowell, G., Zhao, Z.D., Yu, X.H., Mo, X.X., 2015. The nature and
784 history of the Qilian Block in the context of the development of the Greater Tibetan
785 Plateau. Gondwana Research 28, 209–224. https://doi.org/10.1016/j.gr.2014.02.010
786 Kearey, P., Vine, F.J., 1996. Global tectonics. Second edition.
787 Lee, S.R., Cho, M., 2003. Metamorphic and tectonic evolution of the Hwacheon granulite
788 complex, Central Korea: Composite P-T path resulting from two distinct
789 crustal-thickening events. Journal of Petrology 44, 197–225.
790 https://doi.org/10.1093/petrology/44.2.197
791 Li, S., Zhao, S., Liu, X., Cao, H., Yu, Shan, Li, X., Somerville, I., Yu, Shengyao, Suo, Y.,
792 2018. Closure of the Proto-Tethys Ocean and Early Paleozoic amalgamation of
793 microcontinental blocks in East Asia. Earth-Science Reviews 186, 37–75.
794 https://doi.org/10.1016/j.earscirev.2017.01.011
795 Li, X., Niu, M., Yakymchuk, C., Wu, Q., Fu, C., 2019. A paired metamorphic belt in a
796 subduction-to-collision orogen: An example from the South Qilian-North Qaidam
797 orogenic belt, NW China. Journal of Metamorphic Geology 37, 479–508.
798 https://doi.org/10.1111/jmg.12468
799 Li, Y., Tong, X., Zhu, Y., Lin, J., Zheng, J., Brouwer, F.M., 2018a. Tectonic affinity and
800 evolution of the Precambrian Qilian block: Insights from petrology, geochemistry and
801 geochronology of the Hualong Group in the Qilian Orogen, NW China. Precambrian
802 Research 315, 179–200. https://doi.org/10.1016/j.precamres.2018.07.025
803 Li, Y., Zhao, L., Li, Z., Luo, B., Zheng, J., Brouwer, F.M., 2018b. Petrology of Garnet
804 Amphibolites from the Hualong Group: Implications for Metamorphic Evolution of the

Qilian Orogen, NW China. Journal of Earth Science 29, 1102–1115. https://doi.org/10.1007/s12583-018-0850-0

Li, Z., Li, Y., Xiao, W., Zheng, J., Brouwer, F.M., 2020. Geochemical and zircon U-Pb-Hf isotopic study of metasedimentary rocks from the Huangyuan Group of the Central Qilian block (NW China): Implications for paleogeographic reconstruction of Rodinia. Precambrian Research 351. https://doi.org/10.1016/j.precamres.2020.105947

Li, Z., Li, Y., Zhao, L., Zheng, J., Brouwer, F.M., 2019. Petrology and Metamorphic P-T Paths of Metamorphic Zones in the Huangyuan Group, Central Qilian Block, NW China. Journal of Earth Science 30, 1280–1292. https://doi.org/10.1007/s12583-018-0879-0

Liou, J.G., Wang, X., Coleman, R.G., Zhang, Zh.M., Maruyama, S., 1989. Blueschists in major suture zones of China. Tectonics 8, 609–619. https://doi.org/https://doi.org/10.1029/TC008i003p00609

Liou, J.G., Tsujimori, T., Zhang, R.Y., Katayama, I., Maruyama, S., 2004. Global UHP metamorphism and continental subduction/collision: The Himalayan model. International Geology Review 46, 1–27. https://doi.org/10.2747/0020-6814.46.1.1

Lin, Y. H., Cai, J. L., Zhang, L. F., 2009. A Petrological Study of the Maxianshan Group and Its Adjacent Areas in East Qlian Fold Belt, Northwest China. Acta Petrologica et Mineralogica 28, 264–276 (in Chinese with English Abstract).

Liu, Y.-J., Neubauer, F., Genser, J., Takasu, A., Ge, X.-H., Handler, R., 2006. 40Ar/39Ar ages of blueschist facies pelitic schists from Qingshuigou in the Northern Qilian Mountains, western China. Island Arc 15, 187–198. https://doi.org/https://doi.org/10.1111/j.1440-1738.2006.00508.x

827 Liu, Y., Gao, S., Hu, Z., Gao, C., Zong, K., Wang, D., 2010. Continental and Oceanic Crust
828 Recycling-induced Melt-Peridotite Interactions in the Trans-North China Orogen: U-Pb
829 Dating, Hf Isotopes and Trace Elements in Zircons from Mantle Xenoliths. Journal of
830 Petrology 51, 537–571. https://doi.org/10.1093/petrology/egp082
831 Maier-Begandt, D., Comstra, H.S., Molina, S.A., Kruger, N., Ruddiman, C.A., Chen, Y.-L.,
832 Chen, X., Biwer, L.A., Johnstone, S.R., Lohman, A.W., Good, M.E., DeLalio, L.J.,
833 Hong, K., Bacon, H.M., Yan, Z., Sonkusare, S.K., Koval, M., Isakson, B.E., 2021. A
834 venous-specific purinergic signaling cascade initiated by Pannexin 1 regulates
835 TNFalpha-induced increases in endothelial permeability. Science signaling 14.
836 https://doi.org/10.1126/scisignal.aba2940
837 Mancktelow, N.S., Pennacchioni, G., 2004. The influence of grain boundary fluids on the
838 microstructure of quartz-feldspar mylonites. Journal of Structural Geology 26, 47–69.
839 https://doi.org/10.1016/s0191-8141(03)00081-6
840 Meng, F.C., Zhang, J.X., 2008. Contemporaneous of Early Palaeozoic granite and high
841 temperature metamorphism, North Qaidam Mountains, western China: Acta
842 Petrologica Sinica 4, 1585-1594 (in Chinese with English Abstract).
843 Miyashiro, A., 1961. Evolution of metamorphic belts: Journal of Petrology 2, 277–311.
844 Miyashiro, A., 1973. Metamorphism and metamorphic belts. London: Geo. Allen and
845 Unwin Ltd.
846 Passchier, C.W., Trouw, R.A.J., 2005. Microtectonics: Berlin. Springer Verlag, Germany,
847 40–108.

Palin, R.M., Santosh, M., Cao, W., Li, S.-S., Hernandez-Uribe, D., Parsons, A., 2020. Secular change and the onset of plate tectonics on Earth. Earth-Science Reviews 207. https://doi.org/10.1016/j.earscirev.2020.103172

Palin, R.M., Weller, O.M., Waters, D.J., Dyck, B., 2016a. Quantifying geological uncertainty in metamorphic phase equilibria modelling; a Monte Carlo assessment and implications for tectonic interpretations. Geoscience Frontiers 7, 591–607. https://doi.org/10.1016/j.gsf.2015.08.005

Palin, R.M., White, R.W., Green, E.C.R., 2016b. Partial melting of metabasic rocks and the generation of tonalitic-trondhjemitic-granodioritic (TTG) crust in the Archaean: Constraints from phase equilibrium modelling. Precambrian Research 287, 73–90. https://doi.org/10.1016/j.precamres.2016.11.001

Peng, Y., Yu, S., Zhang, J., Li, S., Sun, D., Tong, L., 2017. Early Paleozoic arc magmatism and metamorphism in the northern Qilian Block, western China: A case study of Menyuan-Kekeli. Acta Petrologica Sinica 33, 3925–3941.

Peng, Y.-B., Yu, S.-Y., Zhang, J.-X., Li, S.-Z., Tong, L.-X., Sun, D.-Y., 2017. Early Paleozoic arc magmatism and metamorphism in the northern Qilian Block, western China: Petrological and geochronological constraints. Geological Journal 52, 339–364. https://doi.org/10.1002/gj.3041

Powell, R., White, R.W., Green, E.C.R., Holland, T.J.B., Diener, J.F.A., 2014. On parameterizing thermodynamic descriptions of minerals for petrological calculations. Journal of Metamorphic Geology 32, 245–260. https://doi.org/10.1111/jmg.12070

Qi, X. X., Zhang, J. X., Li, H. B., 2004. Geochronology of the Dextral Strike Ductile Shear Zone in South Margin of the Northern Qilian Mountains and Its Geological Significance. Earth Science Frontiers 11, 469–479 (in Chinese with English Abstract).

Sato, K., Sakai, H., Kawakami, T., 2020. Distribution of ductile deformation around the Main Central Thrust zone at the frontal part of nappe in southeastern Nepal Himalaya. Island Arc 29. https://doi.org/10.1111/iar.12333

Smith, J. V., 1974. Feldspar Minerals. Springer-Verlag, New York.

Song, S., Niu, Y., Su, L., Xia, X., 2013. Tectonics of the North Qilian orogen, NW China. Gondwana Research 23, 1378–1401. https://doi.org/10.1016/j.gr.2012.02.004

Song, S., Wu, Z., Yang, L., Su, L., Xia, X., Wang, C., Dong, J., Zhou, C., Bi, H., 2019. Ophiolite belts and evolution of the Proto-Tethys Ocean in the Qilian Orogen. Acta Petrologica Sinica 35, 2948–2970. https://doi.org/10.18654/1000-0569/2019.10.02

Song, Z. J., Zhang, H. F., Hou, D., Liu, C. F., Liu, W. C., Wu, C., 2018. Discovery and the geological significance of retrograded eclogites from the northern margin of the central Qilian block. Earth science frontiers 26, 233-248 (in Chinese with English abstract).

Stipp, M., Stünitz, H., Heilbronner, R., Schmid, S.M., 2002. The eastern Tonale fault zone: A “natural laboratory” for crystal plastic deformation of quartz over a temperature range from 250 to 700 °C. Journal of Structural Geology 24, 1861–1884. https://doi.org/10.1016/S0191-8141(02)00035-4

889 Sun, Y., Niu, M., Li, X., Wu, Q., Cai, Q., Yuan, X., Li, C., 2020. Petrogenesis and tectonic
890 implications from the Ayishan Group in the South Qilian Belt, NW China. Geological
891 Journal. https://doi.org/10.1002/gj.3851
892 Thompson, A.B., Ridley, J.R., 1987. Tectonic settings of regional metamorphism -
893 Pressure—temperature—time (P—T—t) histories of erogenic belts.
894 Tseng, C.Y., Yang, H.J., Yang, H.Y., Liu, D., Wu, C., Cheng, C.K., Chen, C.H., Ker, C.M.,
895 2009. Continuity of the North Qilian and North Qinling orogenic belts, Central
896 Orogenic System of China: Evidence from newly discovered Paleozoic adakitic rocks.
897 Gondwana Research 16, 285–293. https://doi.org/10.1016/j.gr.2009.04.003
898 Tullis, J., Yund, R.A., 1987. Transition from cataclastic flow to dislocation creep of feldspar:
899 mechanisms and microstructures. Geology 15, 606–609.
900 https://doi.org/10.1130/0091-7613(1987)15<606:TFCFTD>2.0.CO;2
901 Tung, K., Yang, Houng-yi, Liu, D., Zhang, J., Yang, Huai-jen, Shau, Y., Tseng, C., 2013. The
902 Neoproterozoic granitoids from the Qilian block, NW China: Evidence for a link
903 between the Qilian and South China blocks. Precambrian Research 235, 163–189.
904 https://doi.org/10.1016/j.precamres.2013.06.016
905 Tung, K., Yang, Houng-yi, Yang, Huai-jen, Smith, A., Liu, D., Zhang, J., Wu, C., Shau, Y.,
906 Weng, D., Tseng, C., 2016. Magma sources and petrogenesis of the early-middle
907 Paleozoic backarc granitoids from the central part of the Qilian block, NW China.
908 Gondwana Research 38, 197–219. https://doi.org/10.1016/j.gr.2015.11.012

909 Tuzo Wilson, J., 1966. Are the structures of the Caribbean and Scotia arc regions analogous
910 to ice rafting? Earth and Planetary Science Letters 1, 335–338.
911 https://doi.org/10.1016/0012-821X(66)90019-7
912 Wang, C., Li, R.-S., Smithies, R.H., Li, M., Peng, Y., Chen, F.-N., He, S.-P., 2017. Early
913 Paleozoic felsic magmatic evolution of the western Central Qilian belt, Northwestern
914 China, and constraints on convergent margin processes. Gondwana Research 41,
915 301–324. https://doi.org/10.1016/j.gr.2015.12.009
916 Wang, Y., Yang, B., Wang, H., Yu, D., 2016. A discussion on influence factors of quartz
917 c-axis fabrics: An example from mylonite in the Tan-Lu fault zone. 32, 965–975 (in
918 Chinese with English abstract).
919 Wei, C., Shan, Z., Zhang, L., Wang, S., Chang, Z., 1998. Determination and geological
920 significance of the eclogites from the northern Dabie Mountains, central China. Chinese
921 Science Bulletin 43, 253–256. https://doi.org/10.1007/BF02898924
922 Wei, C.J., Song, S.G., 2008. Chloritoid-glaucophane schist in the north Qilian orogen, NW
923 China: phase equilibria and P-T path from garnet zonation. Journal of Metamorphic
924 Geology 26, 301–316. https://doi.org/10.1111/j.1525-1314.2007.00753.x
925 Wei, C.J., Yang, Y., Su, X.L., Song, S.G., Zhang, L.F., 2009. Metamorphic evolution of
926 low-T eclogite from the North Qilian orogen, NW China: evidence from petrology and
927 calculated phase equilibria in the system NCKFMASHO. Journal of Metamorphic
928 Geology 27, 55–70. https://doi.org/10.1111/j.1525-1314.2008.00803.x
929 White, Powell, Holland, Worley, 2000. The effect of TiO2 and Fe2O3 on metapelitic
930 assemblages at greenschist and amphibolite facies conditions: Mineral equilibria

calculations in the system K2O-FeO-MgO-Al2O3-SiO2-H2O-TiO2-Fe2O3. Journal of Metamorphic Geology 18, 497–511. https://doi.org/10.1046/j.1525-1314.2000.00269.x

White, R.W., Powell, R., Clarke, G.L., 2002. The interpretation of reaction textures in Fe-rich metapelitic granulites of the Musgrave Block, Central Australia: Constraints from mineral equilibria calculations in the system. Journal of Metamorphic Geology 20, 41–55. https://doi.org/10.1046/j.0263-4929.2001.00349.x

White, R.W., Powell, R., Holland, T.J.B., Johnson, T.E., Green, E.C.R., 2014. New mineral activity-composition relations for thermodynamic calculations in metapelitic systems. Journal of Metamorphic Geology 32, 261–286. https://doi.org/10.1111/jmg.12071

White, R.W., Powell, R., Halpin, J.A., 2004. Spatially-focussed melt formation in aluminous metapelites from Broken Hill, Australia. Journal of Metamorphic Geology 22, 825–845. https://doi.org/10.1111/j.1525-1314.2004.00553.x

Whitney, D. L., Evans, B. W., 2010. Abbreviations for Names of Rock-Forming Minerals. American Mineralogist 95, 185–187. https://doi.org/10.2138/am.2010.3371

Wu, C., Gao, Y., Frost, B.R., Robinson, P.T., Wooden, J.L., Wu, S., Chen, Q., Lei, M., 2011. An early Palaeozoic double-subduction model for the North Qilian oceanic plate: Evidence from zircon SHRIMP dating of granites. International Geology Review 53, 157–181. https://doi.org/10.1080/00206810902965346

Wu, C., Zuza, A. v, Yin, A., Liu, C., Reith, R.C., Zhang, J., Liu, W., Zhou, Z., 2017. Geochronology and geochemistry of Neoproterozoic granitoids in the central Qilian Shan of northern Tibet: Reconstructing the amalgamation processes and tectonic history of Asia. Lithosphere 9, 609–636. https://doi.org/10.1130/l640.1

Wu, C.L., Yang, J.S., Yang, H.Y., Wooden, J., Shi, R.D., Chen, S.Y., Zheng, Q.G., 2004. Dating of two types of granite from north Qilian, China. Acta Petrologica Sinica 20, 425–432.

Xia, L., Li, X., Ma, Z., Xu, X., Xia, Z., 2011. Cenozoic volcanism and tectonic evolution of the Tibetan plateau. Gondwana Research 19, 850–866. https://doi.org/10.1016/j.gr.2010.09.005

Xia, L.Q., Xia, Z.C., Xu, X.Y., 2003. Magmagenesis in the ordovician backarc basins of the Northern Qilian Mountains, China. Geological Society of America Bulletin 115, 1510–1522. https://doi.org/10.1130/b25269.1

Xiao, W., Windley, B.F., Yong, Y., Yan, Z., Yuan, C., Liu, C., Li, J., 2009. Early Paleozoic to Devonian multiple-accretionary model for the Qilian Shan, NW China. Journal of Asian Earth Sciences 35, 323–333. https://doi.org/10.1016/j.jseaes.2008.10.001

Xu, Y., Du, Y., Cawood, P.A., Yang, J., 2010. Provenance record of a foreland basin: Detrital zircon U-Pb ages from Devonian strata in the North Qilian Orogenic Belt, China. Tectonophysics 495, 337–347. https://doi.org/10.1016/j.tecto.2010.10.001

Xu, Y.J., Du, Y.S., Yang, J.H., Huang, H., 2010. Sedimentary geochemistry and provenance of the Lower and Middle Devonian Laojunshan Formation, the North Qilian Orogenic Belt. Science China Earth Sciences 53, 356–367. https://doi.org/10.1007/s11430-010-0009-zXu, Z., Zhao, Z., Peng, M., Ma, X., Li, H., Zhao, J., 2016. Review of “orogenic plateau.” Acta Petrologica Sinica 32, 3557–3571.

Xu, Z., Zheng, B., Wang, Q., 2021. From accretion to collision: situation and outlook. Acta Geologica Sinica 95, 75–97 (in Chinese with English abstract).

975 Yan, Z., Aitchison, J., Fu, C., Guo, X., Niu, M., Xia, W., Li, J., 2015. Hualong Complex,
976 South Qilian terrane: U-Pb and Lu-Hf constraints on Neoproterozoic micro-continental
977 fragments accreted to the northern Proto-Tethyan margin. Precambrian Research 266,
978 65–85. https://doi.org/10.1016/j.precamres.2015.05.001
979 Yan, Z., Fu, C., Aitchison, J.C., Buckman, S., Niu, M., Cao, B., Sun, Y., Guo, X., Wang, Z.,
980 Zhou, R., 2019. Retro-foreland Basin Development in Response to Proto-Tethyan
981 Ocean Closure, NE Tibet Plateau. Tectonics 38, 4229–4248.
982 https://doi.org/10.1029/2019tc005560
983 Yan, Z., Xiao, W., Aitchison, J.C., Yuan, C., Liu, C., Fu, C., 2021. Age and origin of accreted
984 ocean plate stratigraphy in the North Qilian belt, NE Tibet Plateau: evidence from
985 microfossils and geochemistry of cherts and siltstones. Journal of the Geological
986 Society. https://doi.org/10.1144/jgs2020-231
987 Yang, J.S., Xu, Z.Q., Zhang, J.X., Zhang, Z.M., Liu, F.L., Wu, C.L., 2009. Tectonic setting of
988 main high-and ultrahigh-pressure metamorphic belts in China and adjacent region and
989 discussion on their subduction and exhumation mechanism. Acta Petrologica Sinica 25,
990 1529–1560.
991 Ye, X.-T., Zhang, C.-L., Wang, Q., Wang, G.-D., 2020. Subduction initiation of Proto-Tethys
992 Ocean and back-arc extension in the northern Altun Mountains, northwestern China:
993 Evidence from high-Mg diorites and A-type rhyolites. Lithos 376.
994 https://doi.org/10.1016/j.lithos.2020.105748
995 Ye, Z., Gao, R., Li, Q.S., Zhang, H.S., Shen, X.Z., Liu, X.Z., Gong, C., 2015. Seismic
996 evidence for the North China plate underthrusting beneath northeastern Tibet and its

997 implications for plateau growth. Earth and Planetary Science Letters 426, 109–117.
998 https://doi.org/10.1016/j.epsl.2015.06.024
999 Yin, A., 2010. Cenozoic tectonic evolution of Asia: A preliminary synthesis. Tectonophysics
1000 488, 293–325. https://doi.org/10.1016/j.tecto.2009.06.002
1001 Yong, Y., Xiao, W., Yuan, C., Yan, Z., Li, J., 2008. Geochronology and geochernistry of
1002 Paleozoic granitic plutons from the eastern Central Qilian and their tectonic
1003 implications. Acta Petrologica Sinica 24, 855–866.
1004 Yu, S., Zhang, J., Meng, F., 2007. Geochemical characteristics of low-temperature eclogites
1005 from the subduction-accretionary complex in the North Qilian Mountain. Acta
1006 Petrologica et Mineralogica 26, 101–108 (in Chinese with English abstract).
1007 Yu, S., Li, S., Zhang, J., Peng, Y., Somerville, I., Liu, Y., Wang, Z., Li, Z., Yao, Y., Li, Y.,
1008 2019a. Multistage anatexis during tectonic evolution from oceanic subduction to
1009 continental collision: A review of the North Qaidam UHP Belt, NW China.
1010 Earth-Science Reviews 191, 190–211. https://doi.org/10.1016/j.earscirev.2019.02.016
1011 Yu, S., Peng, Y., Zhang, J., Li, S., Santosh, M., Li, Y., Liu, Y., Gao, X., Ji, W., Lv, P., Li, C.,
1012 Jiang, X., Qi, L., Xie, W., Xu, L., 2021. Tectono-thermal evolution of the Qilian
1013 orogenic system: Tracing the subduction, accretion and closure of the Proto-Tethys
1014 Ocean. Earth-Science Reviews 215, 103547.
1015 https://doi.org/10.1016/j.earscirev.2021.103547
1016 Yu, S., Zhang, J., Li, S., Santosh, M., Li, Y., Liu, Y., Li, X., Peng, Y., Sun, D., Wang, Z., Lv, P.,
1017 2019b. TTG-Adakitic-Like (Tonalitic-Trondhjemitic) Magmas Resulting From Partial
1018 Melting of Metagabbro Under High-Pressure Condition During Continental Collision in

the North Qaidam UHP Terrane, Western China. Tectonics 38, 791–822. https://doi.org/10.1029/2018tc005259

Yu, S., Zhang, J., Li, S., Sun, D., Li, Y., Liu, X., Guo, L., Suo, Y., Peng, Y., Zhao, X., 2017. Paleoproterozoic granulite-facies metamorphism and anatexis in the Oulongbuluke Block, NW China: Respond to assembly of the Columbia supercontinent. Precambrian Research 291, 42–62. https://doi.org/10.1016/j.precamres.2017.01.016

Yu, X.X., 2017. Metamorphism and deformation in the early Paleozoic oceanic subduction tunnel in northern Qilian: Beijing, Peking University (in Chinese with English abstract).

Zhang, J., 2020. The study of subduction channels: Progress, controversies, and challenges. Science China Earth Sciences 63, 1831–1851. https://doi.org/10.1007/s11430-019-9626-5

Zhang, J., Gong, J., Yu, S., Li, H., Hou, K., 2013. Neoarchean-Paleoproterozoic multiple tectonothermal events in the western Alxa block, North China Craton and their geological implication: Evidence from zircon U-Pb ages and Hf isotopic composition. Precambrian Research 235, 36–57. https://doi.org/10.1016/j.precamres.2013.05.002

Zhang, J., Yu, S., Mattinson, C.G., 2017. Early Paleozoic polyphase metamorphism in northern Tibet, China. Gondwana Research 41, 267–289. https://doi.org/10.1016/j.gr.2015.11.009

Zhang, L., Chen, R.-X., Zheng, Y.-F., Hu, Z., Yang, Y., Xu, L., 2016. Geochemical constraints on the protoliths of eclogites and blueschists from North Qilian, northern Tibet. Chemical Geology 421, 26–43. https://doi.org/10.1016/j.chemgeo.2015.11.026

Zhao, G., Cawood, P.A., Li, S., Wilde, S.A., Sun, M., Zhang, J., He, Y., Yin, C., 2012. Amalgamation of the North China Craton: Key issues and discussion. Precambrian Research 222, 55–76. https://doi.org/10.1016/j.precamres.2012.09.016

Zhao, G., Wang, Y., Huang, B., Dong, Y., Li, S., Zhang, G., Yu, S., 2018. Geological reconstructions of the East Asian blocks: From the breakup of Rodinia to the assembly of Pangea. Earth-Science Reviews 186, 262–286. https://doi.org/10.1016/j.earscirev.2018.10.003

Zuza, A. v, Wu, C., Reith, R.C., Yin, A., Li, J., Zhang, J., Zhang, Y., Wu, L., Liu, W., 2018. Tectonic evolution of the Qilian Shan: An early Paleozoic orogen reactivated in the Cenozoic. Geological Society of America Bulletin 130, 881–925. https://doi.org/10.1130/b31721.1

Figure captions

Fig. 1 Geological setting of the research area. (a) Schematic tectonic map of China. (b) Geological map and general cross section of the Qilian Orogen. Details of the granitoids and ophiolites are given in Table S1 (modified after Yan et al., 2015). (c) Geological map of the Huangyuan Group in the Datonghe area (modified after BGMR-QP, 1991). (d) Foliation in the Central Qilian Block.

Fig. 2 (a) Reported *P–T* paths of the *HP/LT* metamorphism in the North Qilian Belt (Zhang et al., 2007; Wei et al., 2009; Yu et al., 2017). (b) Geological map of the Qingshuigou–Xiangzigou area in the North Qilian Belt (modified after Yu, 2017).

Fig. 3 (a) Lithologic–structural map of the Huanyuan Group in the Datonghe area. (b) Dextrally-rotated feldspar porphyroblast. (c) Dextral sense of folding. (d) Dextrally-rotated feldspar. (e) Quartz veins indicating dextral rotation.

Fig. 4 (a) Complex folds cut by north-dipping thrust faults. (b) Multiple stages of thrust faulting.

Fig. 5 Diagram showing the various types of evidence for dextral shearing and rotation during strain (modified after Qi et al., 2004).

Fig. 6 Photomicrographs of mylonites from the shear zones. (a) Dextrally-rotated garnet porphyroclast. (b) Dextrally-rotated amphibole porphyroclast. (c) Dextrally-rotated mica porphyroclast. (d) Mylonite with rotated feldspar porphyroclasts that indicate a dextral sense of shear (feldspar “bookshelf” structures). (e) Dextrally-rotated garnet porphyroclast. (f) *S–C* fabrics that indicate dextral shearing.

Fig. 7 Photomicrographs of mylonites from the dextral ductile shear belt. (a) Mylonite showing dynamic recrystallisation of quartz by bulging + subgrain rotation (BLG + SR) and fracturing of feldspar. (b) Mylonite displaying quartz subgrain rotation. (c) Mylonite with widespread SR of quartz and rotated amphibole. (d) Mylonite exhibiting BLG recrystallisation of quartz and elongate feldspar.

Fig. 8 Lower-hemisphere, equal-area stereographic projections of quartz c-axis fabrics for mylonites from the dextral ductile shear belts in the central segment of the Central Qilian Block.

Fig. 9 (a) Anatexis in gneiss and amphibolite. (b–d) Representative photographs of outcrops and photomicrographs of (b) amphibolite 19ZN06, (c) gneiss 19ZN39 and (d) gneiss 18WJF19.

Fig. 10 (a) Representative BSE image of garnet in sample 18WJF19. (b) Representative chemical composition of the garnet in gneiss 18WJF19. (c) Representative BSE image of feldspar in sample 18WJF19. (b) Feldspar classification diagram after Smith (1974), showing the compositions of plagioclase in gneiss sample 18WJF19. (e) BSE image of kyanite in 18WJF19. (f) Raman spectra for unoriented kyanite in gneiss 18WJF19.

Fig. 11 (a) Concordia diagram and representative cathodoluminescence (CL) images of zircon grains for sample amphibolite 19ZN06. (b) Same as for (a) but for sample gneiss 19ZN39. (c) Same as for (a) but for sample gneiss 18WJF19.

Fig. 12 (a) Calculated *P*–*T* pseudosection for gneiss 18WJF19. (b) *P*–*T* path for gneiss 18WJF19. Mineral abbreviations are from Whitney and Evans (2010). The bulk compositions used for modelling are given in Table 3.

Table captions

Table 1 LA–ICP–MS U–Pb data for zircons from the Huangyuan Group.

Table 2 Results of chemical analyses of garnet and feldspar in gneiss 18WJF19 from the Huangyuan Group.

Table 3 Whole-rock composition of paragneiss 18WJF19 from the Huangyuan Group.

Table 4 Mineral assemblages and microstructures within mylonites from the studied ductile shear belts.

Caption for Supplementary material

Table S1 List of ages of granitoids and ophiolites in the CQB and NQB.

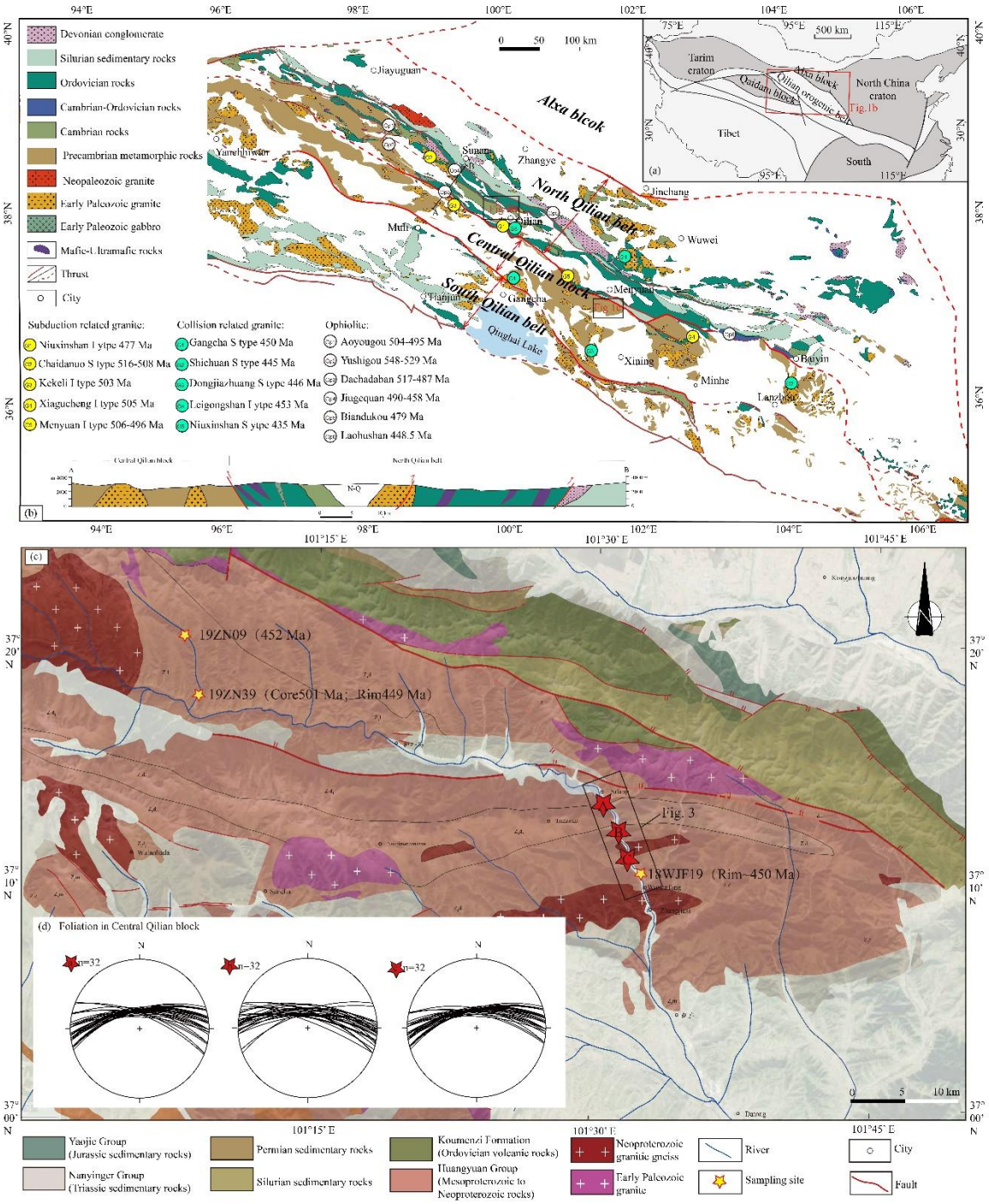
Devonian conglomerate
Silurian sedimentary rocks
Ordovician rocks
Cambrian-Ordovician rocks
Cambrian rocks
Precambrian metamorphic rocks
Neopaleozoic granite
Early Paleozoic granite
Early Paleozoic gabbro
Mafic-Ultramafic rocks
Thrust
City
Alxa blcok
North Qilian belt
Central Qilian block
South Qilian belt
Qinghai Lake
Jiayuguan
Yumenzhen
Suzhou
Zhangye
Jinchang
Wuwei
Mufu
Qilian
Tianjun
Gangcha
Menyuan
Xining
Minhe
Baiyin
Lanzhou
Subduction related granite:
Niuxinshan I ytpe 477 Ma
Chaidanuo S type 516-508 Ma
Kekeli I type 503 Ma
Xiagucheng I type 505 Ma
Menyuan I type 506-496 Ma
Collision related granite:
Gangcha S type 450 Ma
Shichuan S type 445 Ma
Dongjiazhuang S type 446 Ma
Leigongshan I ytpe 453 Ma
Niuxinshan S ytpe 435 Ma
Ophiolite:
Aoyougou 504-495 Ma
Yushigou 548-529 Ma
Dachadaban 517-487 Ma
Jiugequan 490-458 Ma
Biandukou 479 Ma
Laohushan 448.5 Ma
Tarim craton
Qaidam blocks
Alxa block
Qilian orogenic belt
North China craton
Tibet
South
Fig.1b
19ZN09 (452 Ma)
19ZN39 (Core501 Ma; Rim449 Ma)
18WJF19 (Rim~450 Ma)
Fig. 3
(d) Foliation in Central Qilian block
n=32
Yaojie Group (Jurassic sedimentary rocks)
Nanyinger Group (Triassic sedimentary rocks)
Permian sedimentary rocks
Silurian sedimentary rocks
Koumenzi Formation (Ordovician volcanic rocks)
Huangyuan Group (Mesoproterozoic to Neoproterozoic rocks)
Neoproterozoic granitic gneiss
Early Paleozoic granite
River
Sampling site
City
Fault

1108

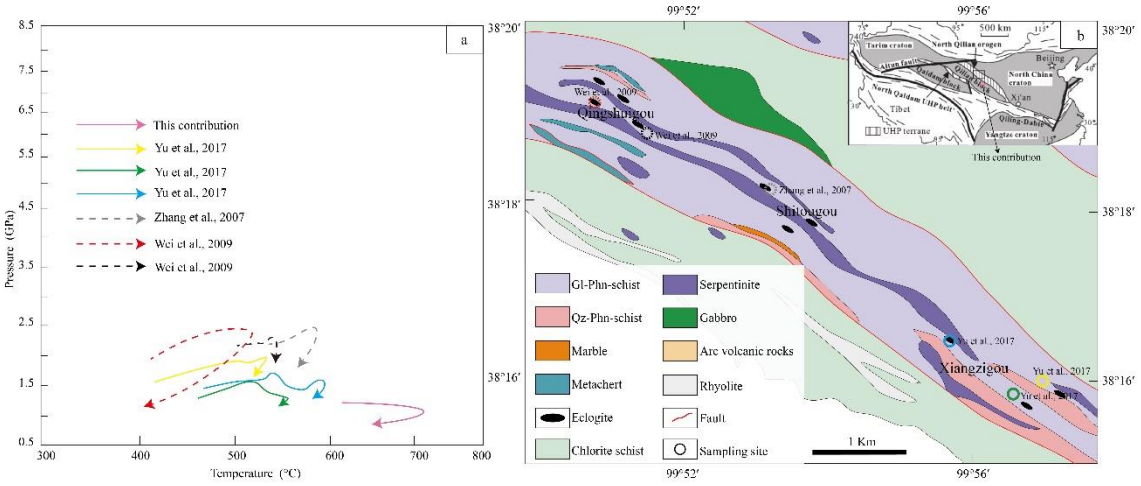
a
This contribution
Yu et al., 2017
Yu et al., 2017
Yu et al., 2017
Zhang et al., 2007
Wei et al., 2009
Wei et al., 2009
Pressure (GPa)
Temperature (°C)
b
Qingshuigou
Shitougou
Xiangzigou
Gl-Phn-schist
Qz-Phn-schist
Marble
Metachert
Eclogite
Chlorite schist
Serpentinite
Gabbro
Arc volcanic rocks
Rhyolite
Fault
Sampling site
1 Km
99°52′
99°56′
38°20′
38°18′
38°16′

1109

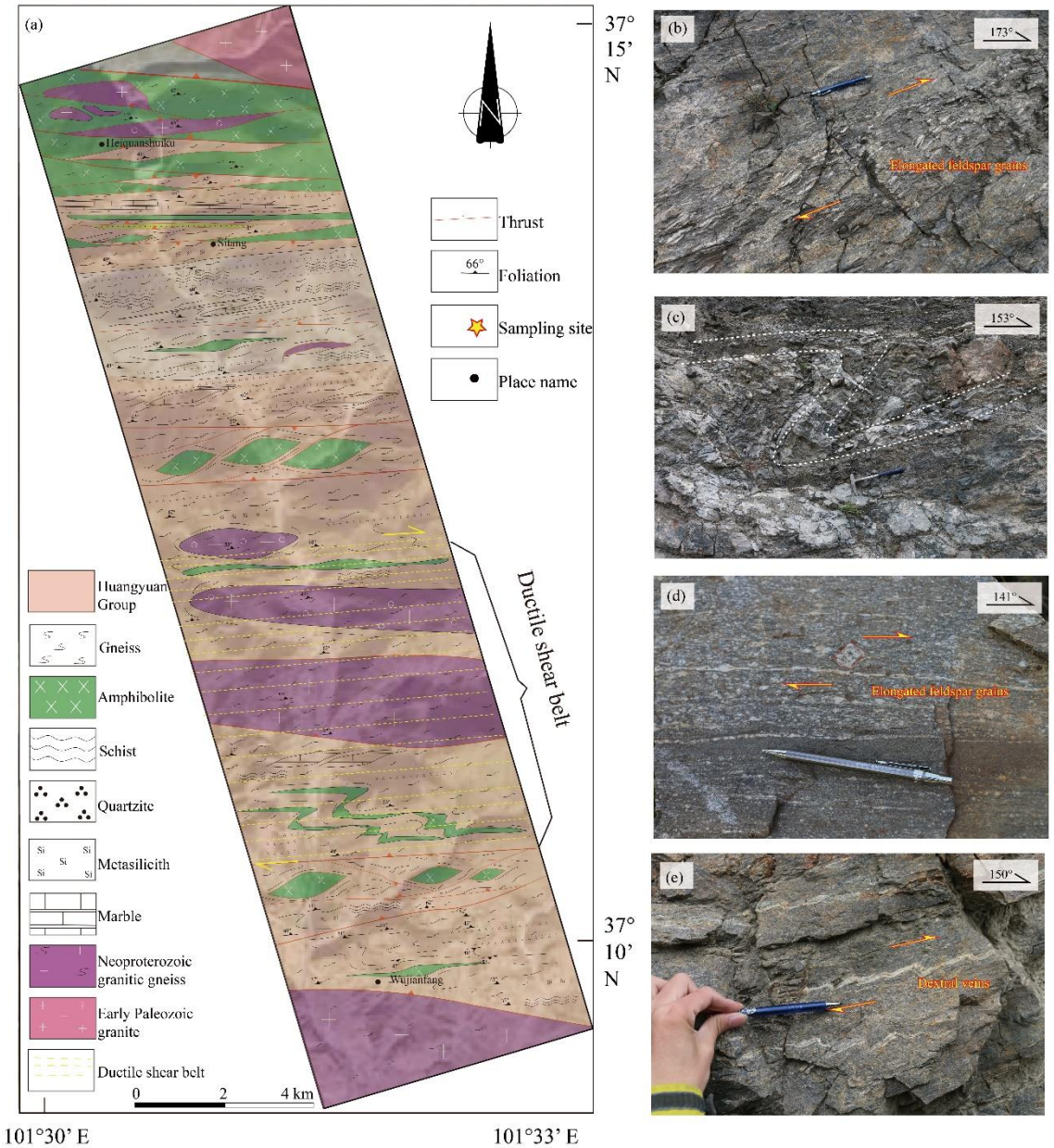
(a)
Heiquanshuiku
Situng
Wujiantang
Huangyuan Group
Gneiss
Amphibolite
Schist
Quartzite
Metasilicith
Marble
Neoproterozoic granitic gneiss
Early Paleozoic granite
Ductile shear belt
Thrust
Foliation
Sampling site
Place name
Ductile shear belt
0 2 4 km
37° 15’ N
37° 10’ N
101°30’ E
101°33’ E
(b)
173°
Elongated feldspar grains
(c)
153°
(d)
141°
Elongated feldspar grains
(e)
150°
Dextral veins

1110

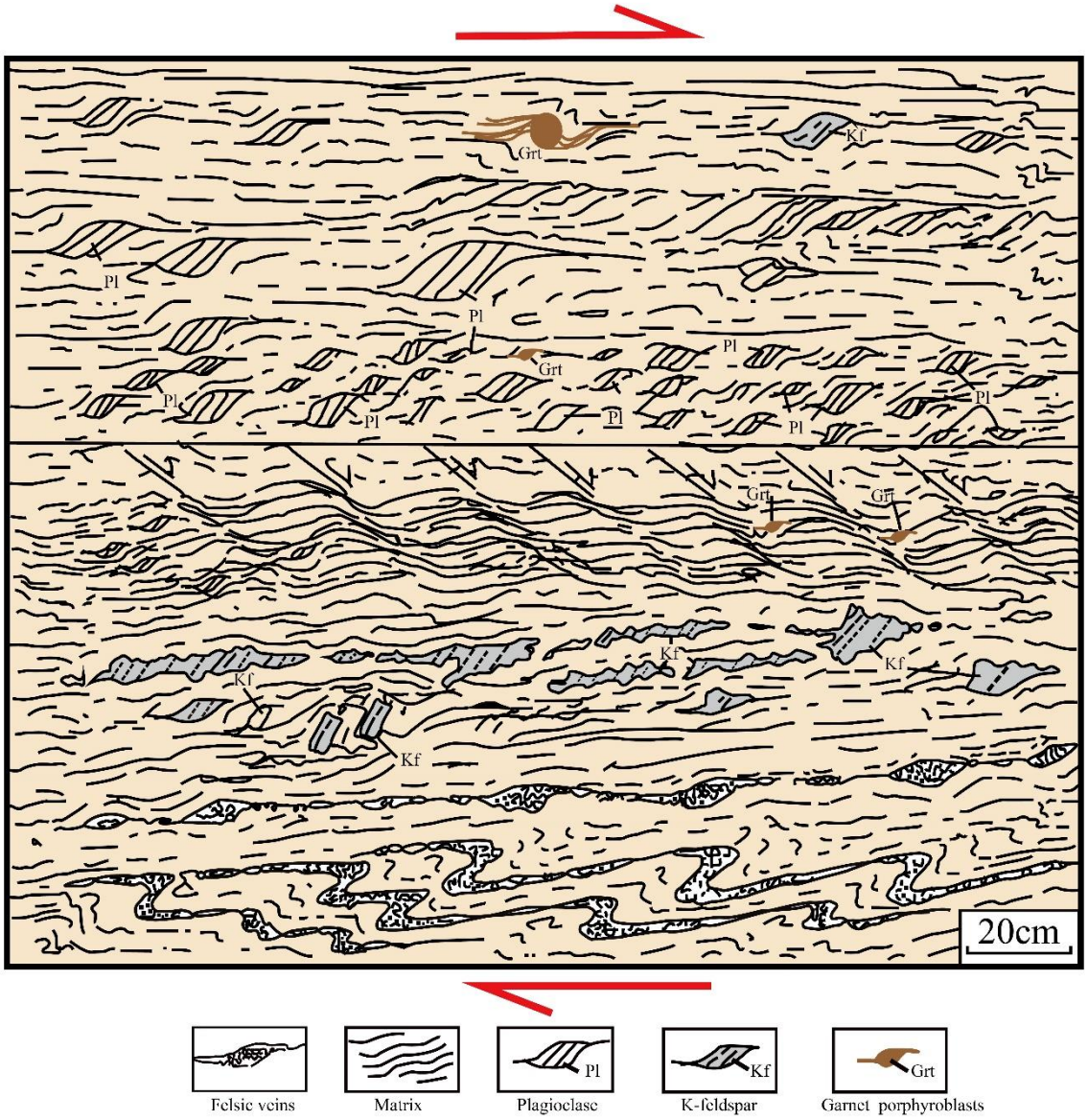
Grt
Kf
Pl
Pl
Grt
Pl
Pl
Pl
Pl
Pl
Pl
Grt
Grt
Kf
Kf
Kf
Kf
20cm
Felsic veins
Matrix
Pl
Plagioclase
Kf
K-feldspar
Grt
Garnet porphyroblasts

1111

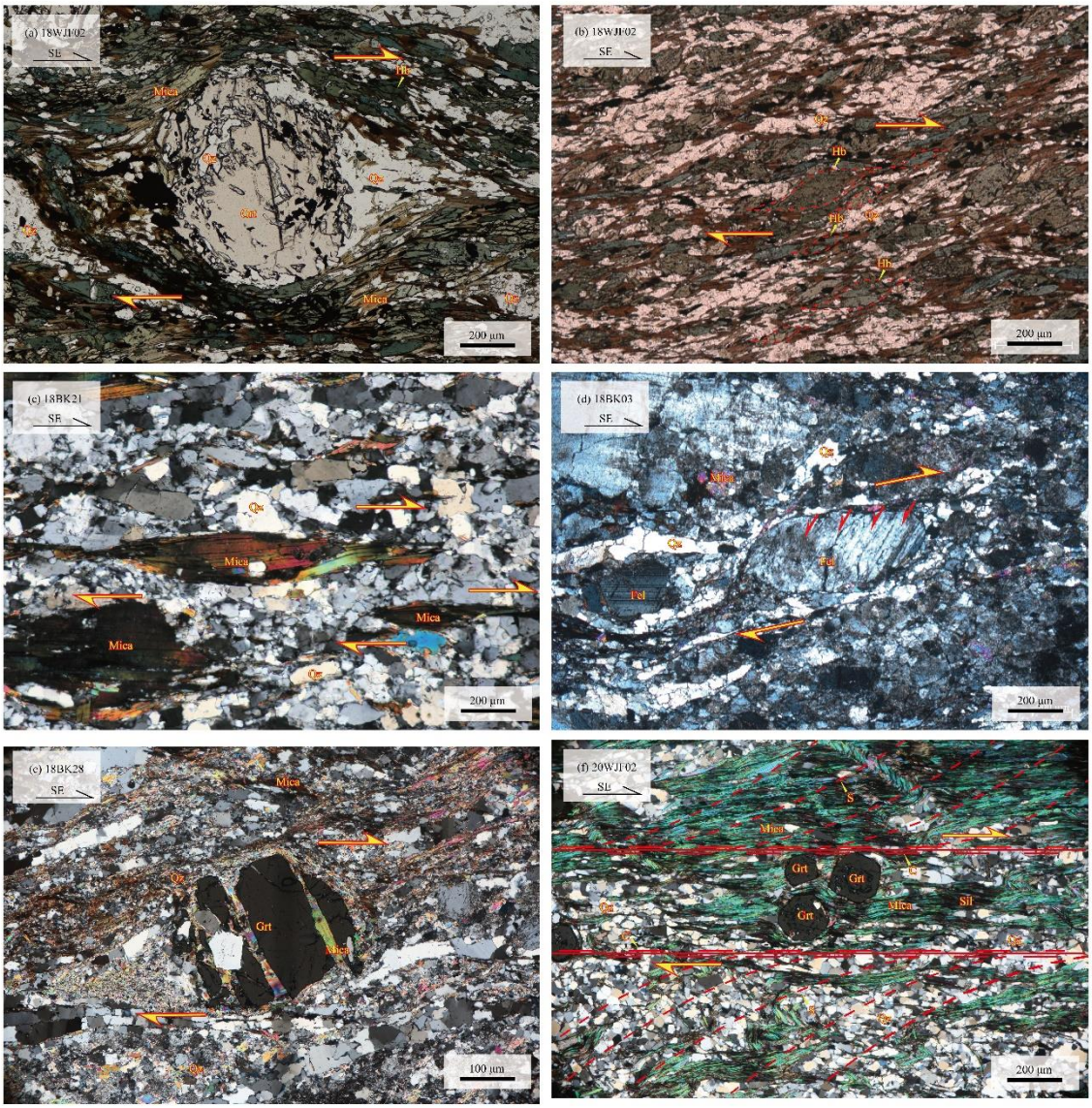
(a) 18WJF02
SE
Hb
Mica
Qz
Grt
Mica
Qz
200 μm
(b) 18WJF02
SE
Qz
Hb
Hb
Qz
Hb
200 μm
(c) 18BK21
SE
Qz
Mica
Mica
Mica
Qz
200 μm
(d) 18BK03
SE
Qz
Mica
Qz
Pl
Pl
200 μm
(e) 18BK28
SE
Mica
Qz
Grt
Mica
Qz
100 μm
(f) 20WJF02
SE
S
Mica
Grt
Grt
Qz
Grt
Micas
Sil
Qz
Qz
Qz
200 μm

1112

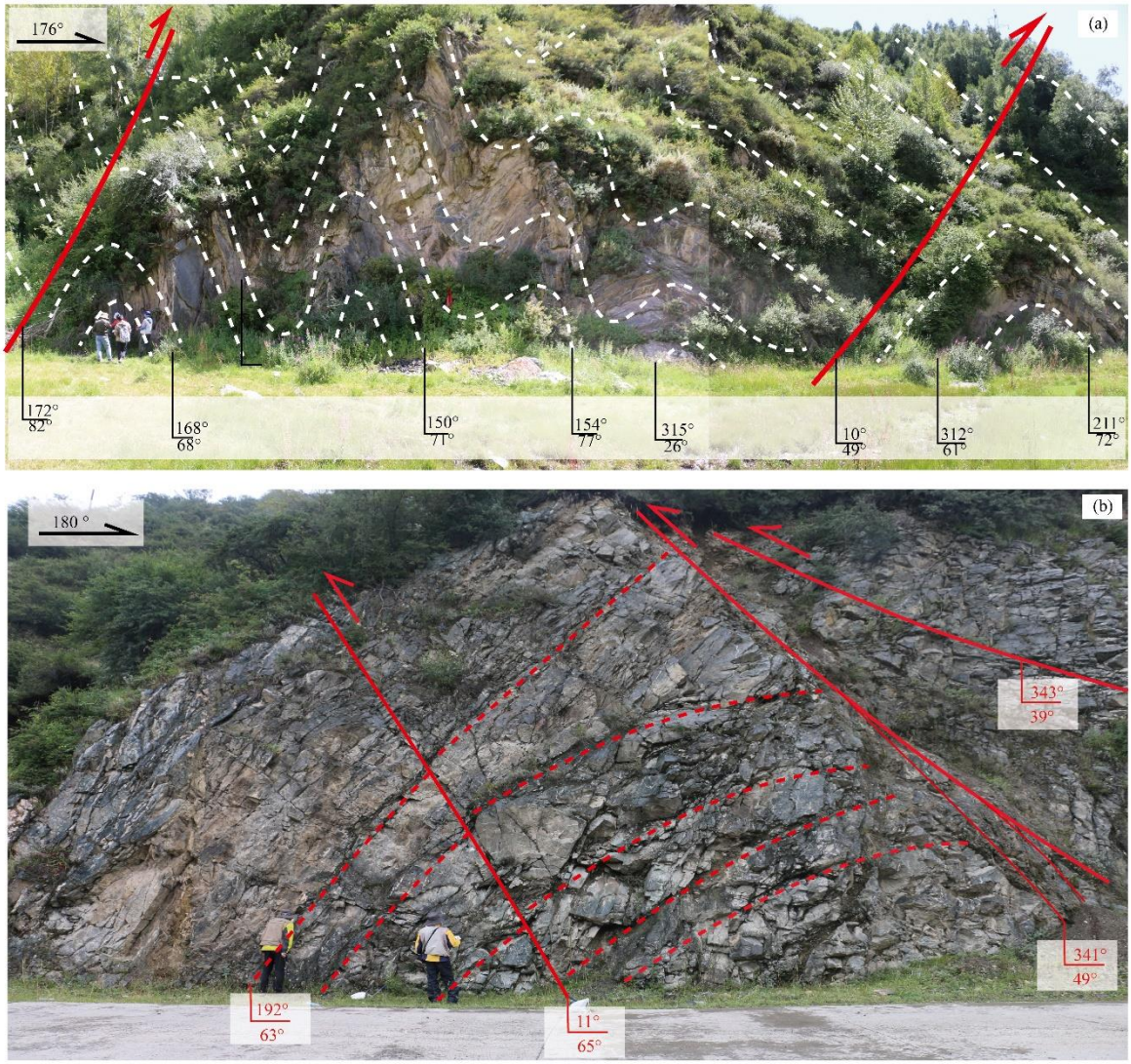
176°
(a)
172°
82°
168°
68°
150°
71°
154°
77°
315°
26°
10°
49°
312°
61°
211°
72°
180 °
(b)
343°
39°
341°
49°
192°
63°
11°
65°

1113

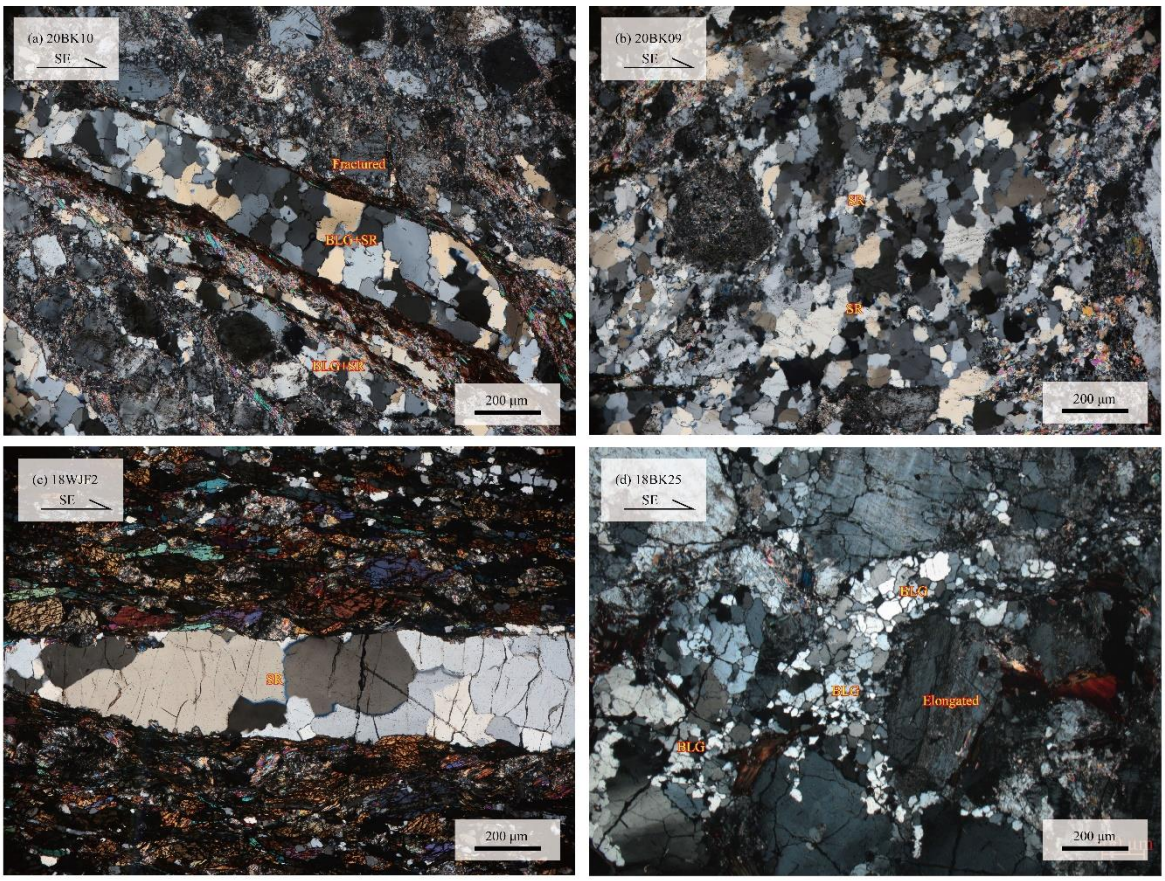
(a) 20BK10
SE
Fractured
BLG+SR
BLG+SR
200 μm
(b) 20BK09
SE
SR
SR
200 μm
(c) 18WJF2
SE
SR
200 μm
(d) 18BK25
SE
BLG
BLG
Elongated
BLG
200 μm

1114

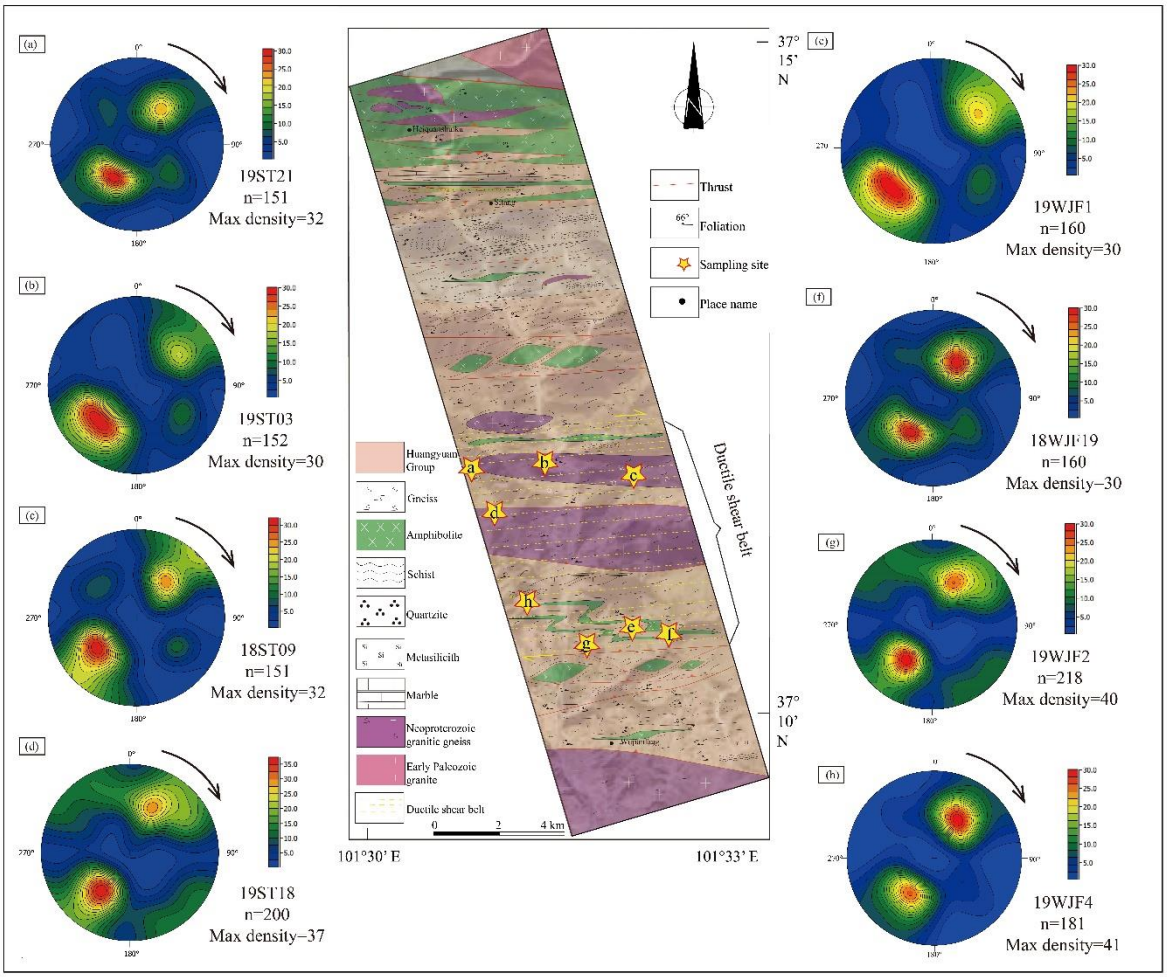
(a)
19ST21
n=151
Max density=32
(b)
19ST03
n=152
Max density=30
(c)
18ST09
n=151
Max density=32
(d)
19ST18
n=200
Max density=37
37° 15' N
37° 10' N
101°30' E
101°33' E
Thrust
Foliation
Sampling site
Place name
Ductile shear belt
Huangyuan Group
Gneiss
Amphibolite
Schist
Quartzite
Metasilicilh
Marble
Neoproterozoic granitic gneiss
Early Paleozoic granite
Ductile shear belt
0 2 4 km
a
b
c
d
e
f
g
h
(c)
19WJF1
n=160
Max density=30
(f)
18WJF19
n=160
Max density=30
(g)
19WJF2
n=218
Max density=40
(h)
19WJF4
n=181
Max density=41

1115

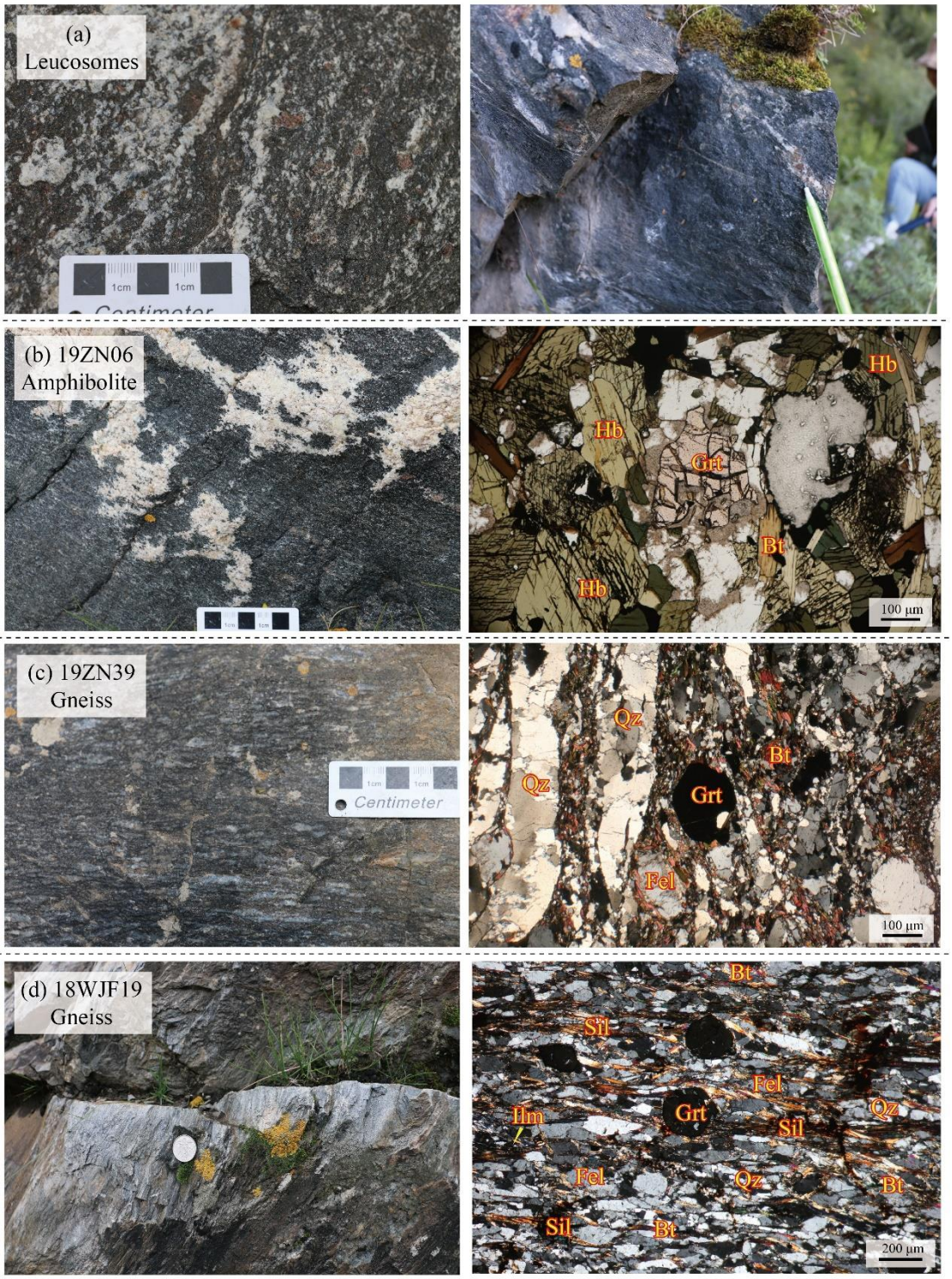
(a)
Leucosomes
(b) 19ZN06
Amphibolite
Hb
Hb
Grt
Bt
Hb
100 μm
(c) 19ZN39
Gneiss
Centimeter
Qz
Bt
Qz
Grt
Fel
100 μm
(d) 18WJF19
Gneiss
Bt
Sil
Fel
Ilm
Grt
Sil
Qz
Fel
Qz
Bt
Sil
Bt
200 μm

1116

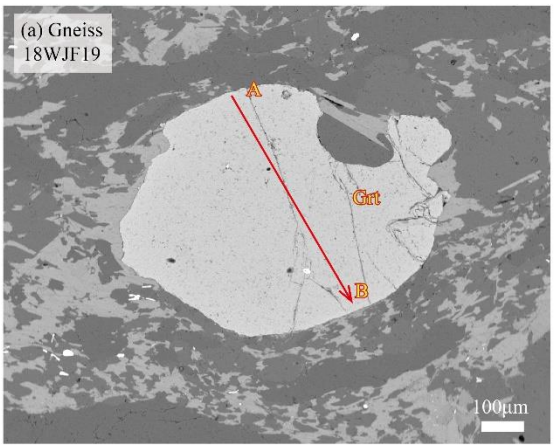
(a) Gneiss
18WJF19
A
Grt
B
100μm

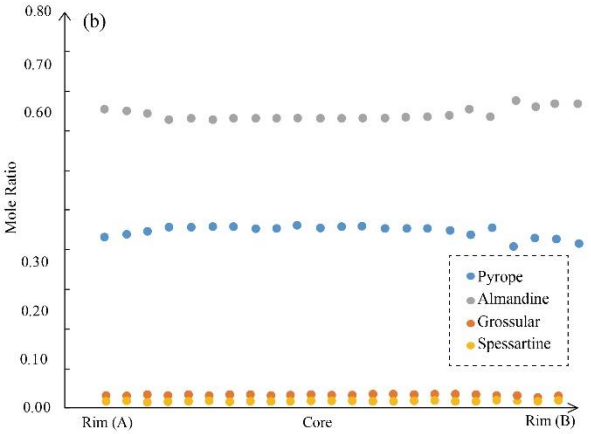
(b)
Mole Ratio
0.80
0.70
0.60
0.30
0.20
0.10
0.00
Pyrope
Almandine
Grossular
Spessartine
Rim (A)
Core
Rim (B)

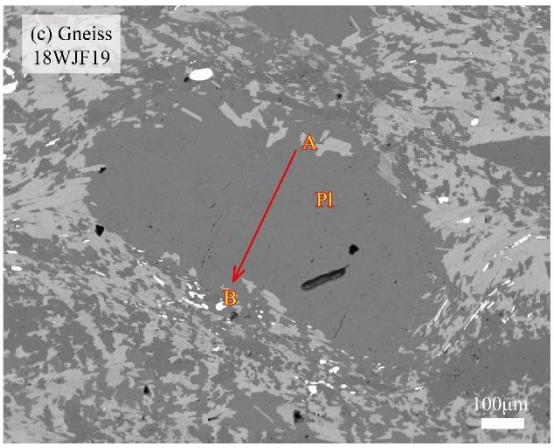
(c) Gneiss
18WJF19
A
Pl
B
100μm

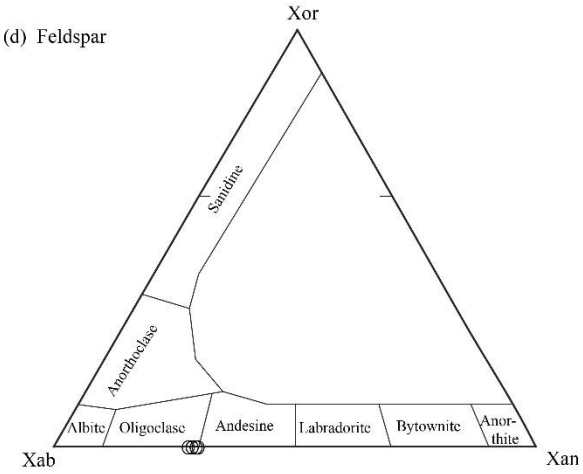
(d) Feldspar
Xor
Xab
Xan
Sanidine
Anorthoclase
Albite
Oligoclase
Andesine
Labradorite
Bytownite
Anor-
thite

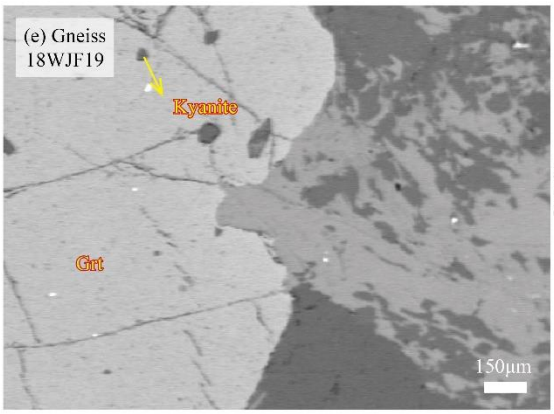
(e) Gneiss
18WJF19
Kyanite
Grt
150μm

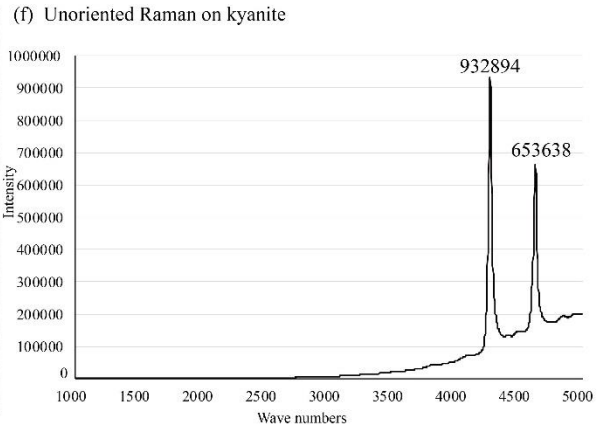
(f) Unoriented Raman on kyanite
932894
653638
Intensity
1000000
900000
800000
700000
600000
500000
400000
300000
200000
100000
0
1000
1500
2000
2500
3000
3500
4000
4500
5000
Wave numbers

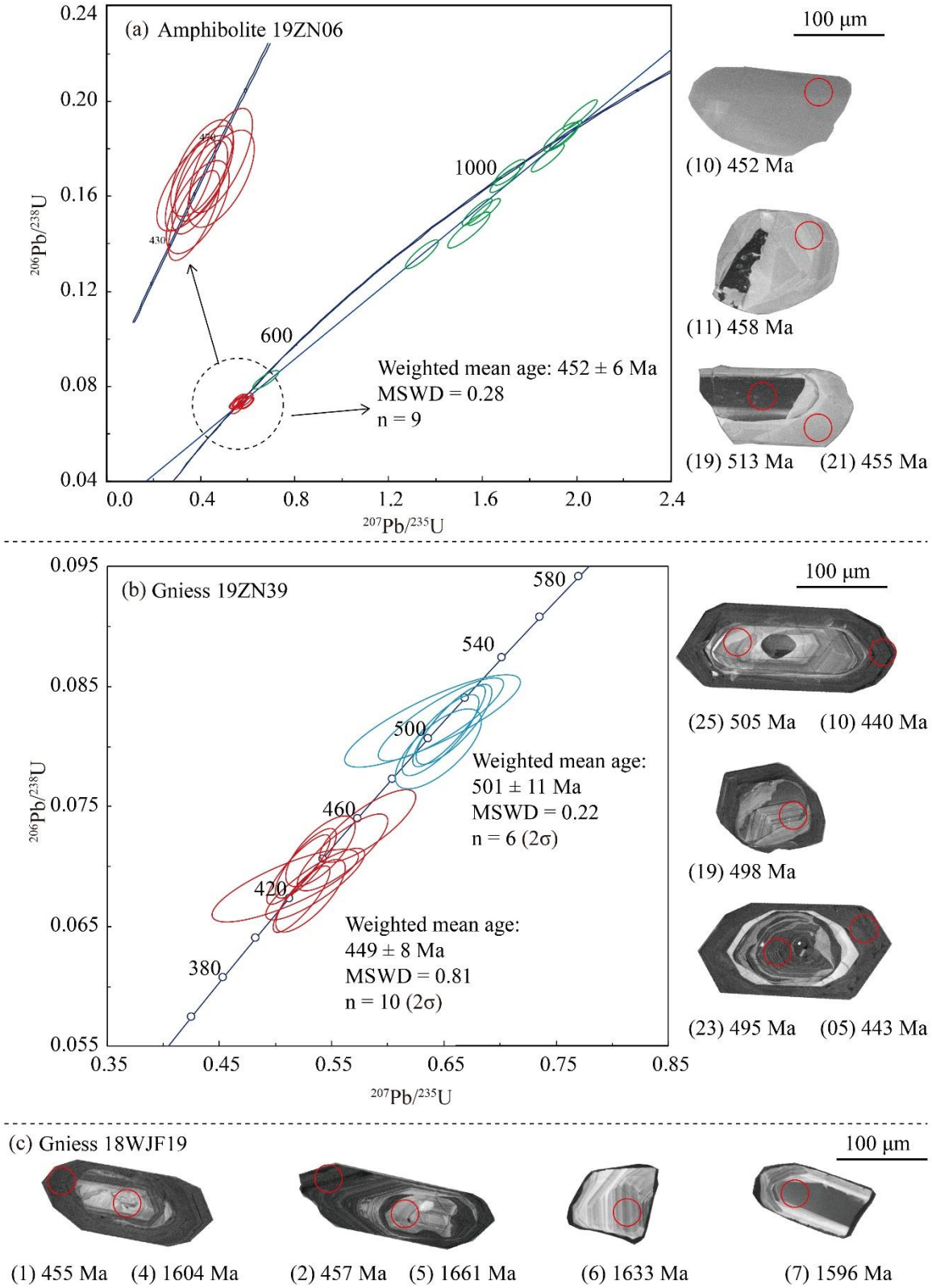
(a) Amphibolite 19ZN06
100 μm
0.24
0.20
0.16
0.12
0.08
0.04
0.0
0.4
0.8
1.2
1.6
2.0
2.4
$^{206}Pb/^{238}U$
$^{207}Pb/^{235}U$
1000
600
430
Weighted mean age: 452 ± 6 Ma
MSWD = 0.28
n = 9
(10) 452 Ma
(11) 458 Ma
(19) 513 Ma
(21) 455 Ma
(b) Gniess 19ZN39
100 μm
0.095
0.085
0.075
0.065
0.055
0.35
0.45
0.55
0.65
0.75
0.85
580
540
500
460
420
380
Weighted mean age:
501 ± 11 Ma
MSWD = 0.22
n = 6 (2σ)
Weighted mean age:
449 ± 8 Ma
MSWD = 0.81
n = 10 (2σ)
(25) 505 Ma
(10) 440 Ma
(19) 498 Ma
(23) 495 Ma
(05) 443 Ma
(c) Gniess 18WJF19
100 μm
(1) 455 Ma
(4) 1604 Ma
(2) 457 Ma
(5) 1661 Ma
(6) 1633 Ma
(7) 1596 Ma

1118

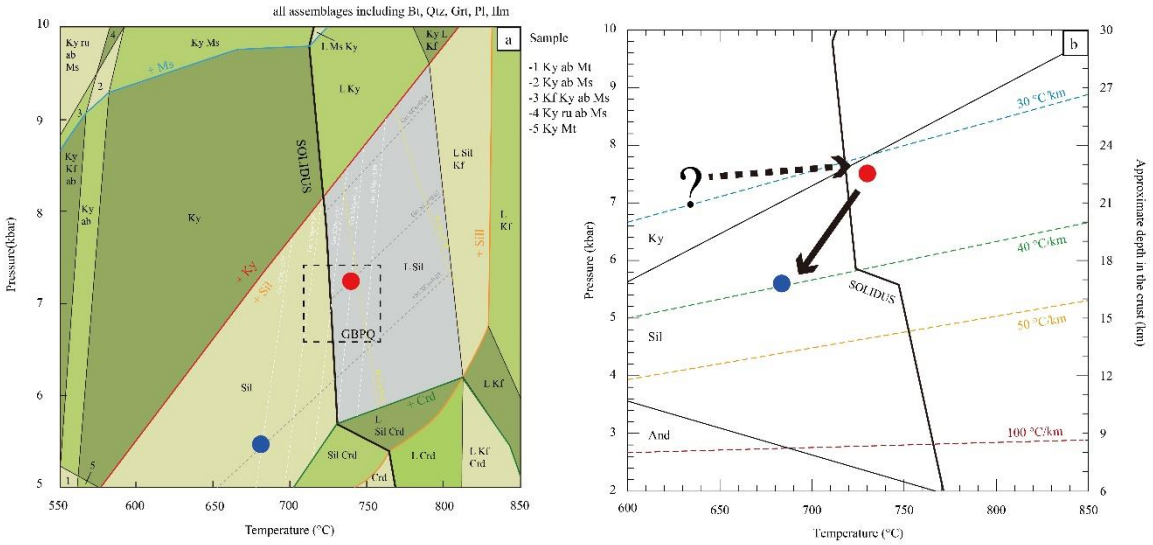
all assemblages including Bt, Qtz, Grt, Pl, Ilm
a
Sample
-1 Ky ab Mt
-2 Ky ab Ms
-3 Kf Ky ab Ms
-4 Ky ru ab Ms
-5 Ky Mt
Ky ru ab Ms
Ky Ms
L Ms Ky
Ky L Kf
+ Ms
L Ky
Ky Kf ab
Ky ab
Ky
SOLIDUS
L Sil Kf
L Kf
+ Ky
+ Sil
+ Sill
L Sil
GBPQ
Sil
+ Crd
L Sil Crd
L Kf
Sil Crd
L Crd
L Kf Crd
Crd
Pressure(kbar)
Temperature (°C)
b
30 °C/km
40 °C/km
50 °C/km
100 °C/km
?
Ky
SOLIDUS
Sil
And
Pressure (kbar)
Approximate depth in the crust (km)
Temperature (°C)

1119

1120 Table 1

Table 1 LA-ICPMS zircon U-Pb data.

Spot number	Th	U	Th/U	CORRECTED RATIOS								CORRECTED AGES (Ma)								
				$^{207}Pb/^{206}Pb$	1s	$^{207}Pb/^{235}U$	1s	$^{206}Pb/^{238}U$	1s	$^{208}Pb/^{232}Th$	1s	$^{207}Pb/^{206}Pb$	1s	$^{207}Pb/^{235}U$	1s	$^{206}Pb/^{238}U$	1s	$^{208}Pb/^{232}Th$	1s	Con.(%)
Sample 19ZN06 (25 spots)																				
19ZN06-01	437.5	656.6	0.67	0.07411	0.00219	1.57655	0.05227	0.15341	0.00451	0.05327	0.00155	1045	32	961	21	920	25	1049	30	96
19ZN06-02	82.13	170.3	0.48	0.05717	0.00226	0.55707	0.02077	0.07091	0.00191	0.02385	0.00080	498	58	450	14	442	11	476	16	98
19ZN06-03	11.13	69.44	0.16	0.05799	0.00279	0.59019	0.02694	0.07329	0.00206	0.02328	0.00129	529	81	471	17	456	12	465	25	97
19ZN06-04	918.1	849.1	1.08	0.07638	0.00215	1.95359	0.05508	0.18583	0.00493	0.05571	0.00156	1105	19	1100	19	1099	27	1096	30	100
19ZN06-05	104.3	250.1	0.42	0.07571	0.00251	1.54204	0.07248	0.14587	0.00611	0.04621	0.00183	1087	44	947	29	878	34	913	35	92
19ZN06-06	21.44	109.4	0.20	0.05648	0.00261	0.58985	0.02549	0.07445	0.00223	0.02455	0.00125	471	71	471	16	463	13	490	25	98
19ZN06-07	130.9	232.5	0.56	0.07366	0.00233	1.71521	0.05337	0.17004	0.00451	0.06446	0.00244	1032	34	1014	20	1012	25	1263	46	100
19ZN06-08	720.1	696.9	1.03	0.07587	0.00219	2.01520	0.05774	0.19428	0.00512	0.05916	0.00168	1092	23	1121	19	1145	28	1162	32	98
19ZN06-09	203.0	339.3	0.60	0.07419	0.00221	1.69576	0.05166	0.16708	0.00450	0.06602	0.00209	1047	29	1007	19	996	25	1292	40	99
19ZN06-10	28.13	148.1	0.19	0.05238	0.00212	0.51736	0.01983	0.07258	0.00198	0.02450	0.00107	302	63	423	13	452	12	489	21	93

19ZN06-11	12.6	118.3	0.11	0.0574	0.00254	0.56976	0.02392	0.07362	0.00203	0.02145	0.00143	508	71	458	15	458	12	429	28	100
19ZN06-12	713.4	687.7	1.04	0.0767	0.00246	1.93416	0.06225	0.18498	0.00496	0.05852	0.00172	1114	36	1093	22	1094	27	1149	33	100
19ZN06-13	1953.9	2033.5	0.96	0.0772	0.00254	1.93144	0.05972	0.18272	0.00479	0.05823	0.00171	1126	33	1092	21	1082	26	1144	33	99
19ZN06-14	94.0	445.6	0.21	0.0561	0.00246	0.56672	0.02509	0.07398	0.00206	0.02406	0.00105	456	78	456	16	460	12	481	21	99
19ZN06-15	126.3	499.7	0.25	0.0568	0.00232	0.56419	0.02263	0.07274	0.00200	0.02325	0.00092	485	66	454	15	453	12	465	18	100
19ZN06-16	127.6	653.6	0.20	0.0587	0.00231	0.59957	0.02187	0.07304	0.00203	0.02459	0.00097	558	53	477	14	454	12	491	19	95
19ZN06-17	179.8	564.3	0.32	0.0584	0.00466	0.70256	0.05018	0.08718	0.00310	0.02701	0.00091	547	180	540	30	539	18	539	18	100
19ZN06-18	3995.2	5398.0	0.74	0.0706	0.00217	1.34228	0.05754	0.13565	0.00504	0.05157	0.00186	947	45	864	25	820	29	1016	36	95
19ZN06-19	263.2	1128.8	0.23	0.0593	0.00446	0.67766	0.04431	0.08283	0.00307	0.02561	0.00092	580	169	525	27	513	18	511	18	98
19ZN06-20	4862.9	4176.5	1.16	0.0739	0.00234	1.60647	0.05525	0.15334	0.00474	0.05344	0.00208	1040	31	973	22	920	26	1052	40	94
19ZN06-21	114.2	507.8	0.22	0.0554	0.00340	0.55783	0.03045	0.07300	0.00203	0.02276	0.00062	429	141	450	20	454	12	455	12	99
19ZN06-22	2210.4	2817.6	0.78	0.0770	0.00224	1.87746	0.05802	0.17602	0.00488	0.05638	0.00166	1122	28	1073	20	1045	27	1109	32	97
19ZN06-23	306.7	683.6	0.45	0.0605	0.00620	0.61095	0.06353	0.07322	0.00202	0.02381	0.00085	624	225	484	40	456	12	476	17	94
19ZN06-24	193.2	542.4	0.36	0.0549	0.00211	0.55259	0.02041	0.07294	0.00200	0.02415	0.00095	412	56	447	13	454	12	482	19	98

19ZN06-25	89.4	358.5	0.25	0.05706	0.00267	0.57204	0.02541	0.07101	0.00199	0.02637	0.00111	494	78	459	16	442	12	526	22	96
Sample 19ZN39 (27 spots)																				
19ZN39-01	87.2	300	0.29	0.05470	0.00200	0.54021	0.02064	0.07125	0.00195	0.02337	0.00084	400	61	439	14	444	12	467	16	99
19ZN39-02	27.5	73.6	0.37	0.06725	0.00338	0.66788	0.03207	0.07220	0.00215	0.03042	0.00129	846	80	480	20	449	13	606	25	93
19ZN39-03	211	765	0.28	0.05625	0.00178	0.52305	0.01684	0.06727	0.00185	0.02049	0.00065	462	38	427	11	420	11	410	13	98
19ZN39-04	53.7	581	0.09	0.05886	0.00276	0.60537	0.02262	0.07459	0.00211	0.02309	0.00065	562	105	481	14	464	13	461	13	96
19ZN39-05	142	1040	0.14	0.05705	0.00317	0.55987	0.02645	0.07118	0.00209	0.02211	0.00064	493	126	451	17	443	13	442	13	98
19ZN39-06	1129	1975	0.57	0.06239	0.00189	0.64981	0.01978	0.07485	0.00209	0.02679	0.00082	688	27	508	12	465	13	534	16	91
19ZN39-07	84.6	167	0.51	0.05708	0.00239	0.53369	0.02049	0.06744	0.00198	0.02217	0.00085	495	56	434	14	421	12	443	17	97
19ZN39-08	110	363	0.30	0.05401	0.00190	0.52687	0.01772	0.07029	0.00192	0.02304	0.00077	371	45	430	12	438	12	460	15	98
19ZN39-09	648	2246	0.29	0.05663	0.00346	0.53531	0.02885	0.06856	0.00198	0.02132	0.00060	477	139	435	19	427	12	426	12	98
19ZN39-10	217	274	0.79	0.06039	0.00774	0.59035	0.07870	0.07056	0.00194	0.02274	0.00074	617	294	471	50	440	12	455	15	93
19ZN39-11	172	2810	0.06	0.05416	0.00243	0.52084	0.01852	0.06974	0.00191	0.02180	0.00061	378	104	426	12	435	12	436	12	98
19ZN39-12	1954	2973	0.66	0.05976	0.00175	0.61961	0.01821	0.07498	0.00204	0.02647	0.00078	595	24	490	11	466	12	528	15	95
19ZN39-	425	123	0.3	0.0580	0.001	0.5513	0.017	0.0687	0.001	0.0221	0.000	532	36	446	1	429	1	443	1	96

13		4	4	7	80	7	17	8	83	8	67				1		1		3	
19ZN39-14	111	502	0.22	0.05792	0.00321	0.58842	0.02838	0.07368	0.00201	0.02285	0.00060	527	125	470	18	458	12	457	12	97
19ZN39-15	145	209	0.69	0.05395	0.00482	0.50868	0.04289	0.06838	0.00201	0.02139	0.00054	369	204	418	29	426	12	428	11	98
19ZN39-16	246	846	0.29	0.05839	0.00182	0.59491	0.01829	0.07372	0.00202	0.02383	0.00073	544	31	474	12	459	12	476	14	97
19ZN39-17	838	1299	0.65	0.05870	0.00171	0.63036	0.01931	0.07747	0.00211	0.02624	0.00074	556	31	496	12	481	13	523	15	97
19ZN39-18	1290	1049	1.23	0.05850	0.00173	0.62908	0.01908	0.07765	0.00210	0.02400	0.00069	548	31	496	12	482	13	479	14	97
19ZN39-19	173	486	0.36	0.05677	0.00193	0.61247	0.02089	0.08028	0.00371	0.02527	0.00082	483	30	485	13	498	22	504	16	97
19ZN39-20	735	1315	0.56	0.05872	0.00172	0.63120	0.01932	0.07762	0.00218	0.02589	0.00077	557	27	497	12	482	13	517	15	97
19ZN39-21	740	1264	0.59	0.06143	0.00183	0.67186	0.02060	0.07907	0.00229	0.02719	0.00079	654	22	522	13	491	14	542	16	94
19ZN39-22	776	1231	0.63	0.05651	0.00486	0.63990	0.05139	0.08213	0.00254	0.02554	0.00069	472	197	502	23	509	15	510	14	99
19ZN39-23	154	414	0.37	0.05980	0.00202	0.66243	0.02264	0.07976	0.00223	0.02577	0.00084	596	44	516	14	495	13	514	17	96
19ZN39-24	413	892	0.46	0.05926	0.00186	0.66697	0.02112	0.08106	0.00222	0.02728	0.00085	577	35	519	13	502	13	544	17	97
19ZN39-25	555	651	0.85	0.05901	0.00197	0.66707	0.02226	0.08146	0.00219	0.02634	0.00079	567	44	519	14	505	13	525	16	97
19ZN39-26	157	201	0.78	0.05887	0.00242	0.64492	0.02550	0.07947	0.00220	0.02617	0.00084	562	63	505	16	493	13	522	17	98
19ZN39-	474	114	0.4	0.0570	0.003	0.6473	0.036	0.0822	0.002	0.0255	0.000	495	14	507	2	510	1	510	1	99

27		0	2	8	63	8	94	6	31	5	66		4		3		4		3	
Sample 18WJF19 (7spots)																				
18WJF19-01	15.3	786	0.02	0.05877	0.00319	0.59321	0.02801	0.07321	0.00197	0.02266	0.00059	559	122	473	18	455	12	453	12	96
18WJF19-02	24.1	1290	0.02	0.05644	0.00237	0.57774	0.02504	0.07343	0.00206	0.00466	0.00286	470	75	463	16	457	12	94	58	99
18WJF19-03	9.56	654	0.01	0.05556	0.00242	0.54972	0.01925	0.07176	0.00185	0.02236	0.00061	435	99	445	13	447	11	447	12	100
18WJF19-04	357	1158	0.31	0.09891	0.00564	3.41720	0.16101	0.25057	0.00803	0.07326	0.00230	1604	109	1508	37	1441	41	1429	43	95
18WJF19-05	302	515	0.59	0.10203	0.00588	3.81347	0.19115	0.27109	0.00771	0.07900	0.00215	1661	110	1596	40	1546	39	1537	40	97
18WJF19-06	285	423	0.67	0.10046	0.00334	4.09955	0.13460	0.29493	0.00785	0.08314	0.00276	1633	45	1654	27	1666	39	1614	52	99
18WJF19-07	138	179	0.77	0.09852	0.00352	3.83803	0.15467	0.27955	0.00867	0.08128	0.00291	1596	50	1601	32	1589	44	1579	54	99

1123 Table 2

Table 2 EPMA data for metamorphic rocks from the Huangyuan Group.

Garnet Weight % oxides (Number of ions on basis of 12 oxygen atoms.)																						
	G1-1	G1-2	G1-3	G1-4	G1-5	G1-6	G1-7	G1-8	G1-9	G1-10	G1-11	G1-12	G1-13	G1-14	G1-15	G1-16	G1-17	G1-18	G1-19	G1-20	G1-21	G1-22	G1-23
SiO2	38.27	38.09	38.15	37.95	37.93	38.01	37.84	38.02	37.81	38.24	38.13	38.29	37.68	38.35	38.30	38.25	38.07	38.54	38.24	38.12	38.39	37.97	38.13
Na2O	0.04	0.02	0.03	0.02	0.01	0.00	0.00	0.01	0.01	0.00	0.03	0.00	0.01	0.00	0.00	0.01	0.03	0.00	0.01	0.00	0.00	0.02	0.00
MgO	9.77	9.82	10.04	10.18	10.25	10.25	10.38	10.36	10.32	10.41	10.39	10.36	10.49	10.29	10.24	10.33	10.20	10.15	10.18	9.05	9.75	9.71	9.55
Al2O3	20.05	20.69	20.57	20.56	20.67	20.79	20.70	20.55	20.82	20.03	20.04	20.29	20.64	20.30	20.69	20.12	20.77	19.06	20.63	20.10	19.22	19.62	19.17
Cr2O3	0.07	0.00	0.02	0.05	0.03	0.05	0.06	0.00	0.06	0.00	0.02	0.00	0.02	0.02	0.02	0.00	0.01	0.01	0.00	0.03	0.04	0.03	0.04
K2O	0.04	0.00	0.01	0.02	0.01	0.01	0.00	0.01	0.03	0.01	0.00	0.00	0.01	0.00	0.00	0.00	0.00	0.00	0.00	0.00	0.00	0.00	0.01
CaO	0.92	0.86	0.97	0.95	0.92	0.91	0.94	0.97	0.92	0.93	0.96	0.94	0.92	0.99	0.97	0.92	0.96	0.99	0.96	0.94	0.93	0.80	0.87
TiO2	0.00	0.03	0.02	0.00	0.00	0.04	0.00	0.01	0.00	0.00	0.02	0.00	0.00	0.00	0.00	0.00	0.00	0.02	0.00	0.00	0.01	0.05	0.00
MnO	0.59	0.62	0.53	0.59	0.55	0.59	0.53	0.60	0.53	0.61	0.60	0.58	0.58	0.59	0.60	0.57	0.63	0.58	0.61	0.64	0.61	0.69	0.72
FeO	29.97	29.70	29.78	28.85	29.20	28.84	29.47	29.74	29.49	29.44	29.72	29.45	29.62	29.52	29.49	29.75	29.63	30.70	28.78	30.83	31.09	31.11	31.44
Total	99.72	99.82	100.11	99.16	99.57	99.50	99.92	100.26	99.96	99.67	99.91	99.92	99.95	100.05	100.30	99.96	100.30	100.04	99.40	99.71	100.03	100.01	99.93

Si	2.89	2.86	2.86	2.86	2.85	2.86	2.84	2.85	2.84	2.88	2.87	2.87	2.83	2.88	2.86	2.87	2.85	2.91	2.87	2.89	2.90	2.87	2.89
Ti	0.00	0.00	0.00	0.00	0.00	0.00	0.00	0.00	0.00	0.00	0.00	0.00	0.00	0.00	0.00	0.00	0.00	0.00	0.00	0.00	0.00	0.00	0.00
Al	1.78	1.83	1.82	1.83	1.83	1.84	1.83	1.82	1.84	1.78	1.78	1.80	1.83	1.79	1.82	1.78	1.83	1.70	1.83	1.79	1.71	1.75	1.72
Cr	0.00	0.00	0.00	0.00	0.00	0.00	0.00	0.00	0.00	0.00	0.00	0.00	0.00	0.00	0.00	0.00	0.00	0.00	0.00	0.00	0.00	0.00	0.00
Fe3	0.30	0.30	0.29	0.30	0.30	0.30	0.30	0.29	0.30	0.30	0.30	0.30	0.30	0.29	0.29	0.30	0.29	0.30	0.30	0.30	0.30	0.30	0.30
Fe2	1.89	1.87	1.87	1.82	1.84	1.81	1.85	1.86	1.85	1.85	1.87	1.85	1.86	1.85	1.84	1.87	1.86	1.94	1.81	1.95	1.97	1.97	2.00
Mn	0.04	0.04	0.03	0.04	0.04	0.04	0.03	0.04	0.03	0.04	0.04	0.04	0.04	0.04	0.04	0.04	0.04	0.04	0.04	0.04	0.04	0.04	0.05
Mg	1.10	1.10	1.12	1.15	1.15	1.15	1.16	1.16	1.15	1.17	1.17	1.16	1.18	1.15	1.14	1.16	1.14	1.14	1.14	1.02	1.10	1.10	1.08
Ca	0.07	0.07	0.08	0.08	0.07	0.07	0.08	0.08	0.07	0.08	0.08	0.08	0.07	0.08	0.08	0.07	0.08	0.08	0.08	0.08	0.08	0.07	0.07
Na	0.01	0.00	0.00	0.00	0.00	0.00	0.00	0.00	0.00	0.00	0.00	0.00	0.00	0.00	0.00	0.00	0.00	0.00	0.00	0.00	0.00	0.00	0.00
K	0.00	0.00	0.00	0.00	0.00	0.00	0.00	0.00	0.00	0.00	0.00	0.00	0.00	0.00	0.00	0.00	0.00	0.00	0.00	0.00	0.00	0.00	0.00
XPrp	0.35	0.36	0.36	0.37	0.37	0.37	0.37	0.37	0.37	0.37	0.37	0.37	0.37	0.37	0.37	0.37	0.37	0.36	0.37	0.33	0.35	0.35	0.34
XGrs	0.02	0.02	0.03	0.03	0.02	0.02	0.02	0.02	0.02	0.02	0.02	0.02	0.02	0.03	0.03	0.02	0.02	0.03	0.03	0.02	0.02	0.02	0.02
XAlm	0.61	0.61	0.60	0.59	0.59	0.59	0.59	0.59	0.59	0.59	0.59	0.59	0.59	0.59	0.59	0.60	0.60	0.61	0.59	0.63	0.62	0.62	0.63

XSps	0.01	0.01	0.01	0.01	0.01	0.01	0.01	0.01	0.01	0.01	0.01	0.01	0.01	0.01	0.01	0.01	0.01	0.01	0.01	0.01	0.01	0.01	0.01
XMg	0.35	0.36	0.36	0.37	0.37	0.37	0.37	0.37	0.37	0.37	0.37	0.37	0.37	0.37	0.37	0.37	0.37	0.36	0.37	0.33	0.35	0.35	0.34
XCa	0.02	0.02	0.03	0.03	0.02	0.02	0.02	0.02	0.02	0.02	0.02	0.02	0.03	0.03	0.02	0.02	0.03	0.03	0.02	0.02	0.02	0.02	

1124

1125

Table 3

Table 3 Whole-rock composition from the Huangyuan Group.		
Sample		18WJF19
Rock type		Gneiss
Major elements (wt %)	SiO_2	71.20
	TiO_2	1.27
	Al_2O_3	12.31
	Fe_2O_3	1.00
	MnO	0.05
	MgO	2.29
	CaO	1.27
	Na_2O	2.99
	K_2O	1.96
	P_2O_5	0.05
	LOI	0.94
	FeO	5.4
	Total	100.73

1129 Table 4

Table 4 Mineral assemblages and microstructures within mylonites from the studied ductile shear belts

Sample No.	Rock type	Mineral assemblage	Quartz	Feldspar	Estimated T (°C)
18CHH15	Mylonite	Feld+Qtz+Bt	SR	Elongated	400–500
18CHH20	Mylonite	Grt+Feld+Qtz+Ms	SR	Elongated	400–500
20BK10	Mylonite	Grt+Feld+Qtz+Ms	BLG + SR	Fractured	350–400
18ST1	Protomylonite	Grt+Feld+Qtz+Ms+Bt	SR	Elongated	400–500
18ST3	Mylonite	Feld+Qtz+Ms	SR	Elongated	400–450
18ST12	Protomylonite	Feld+Qtz+Ms+Bt	SR	Elongated	450–500
20BK09	Mylonite	Grt+Feld+Qtz	SR	Elongated	450–500
18BK14	Mylonite	Grt+Feld+Qtz+Bt	SR	Elongated	450–500
18BK25	Mylonite	Feld+Qtz+Bt	SR	Elongated	400–450
18WJF2	Mylonite	Grt+Feld+Qtz+Amp+Bt	SR	Elongated	400–450
18WJF18	Mylonite	Grt+Feld+Qtz+Bt+Sil	BLG + SR	Fractured	350–400
18WJF19	Mylonite	Grt+Feld+Qtz+Bt+Sil	BLG + SR	Fractured	350–400
18WJF20	Protomylonite	Feld+Qtz	SR	Elongated	400–450

1130 Table S1

Table S1. List of ages of granitoids and ophiolite

location	Age (Ma)	References
Granitoids		
Chaidanuo	516-508	Chen et al., 2014
Menyuan	506-496	Peng et al., 2017
Kekeli	512	Wu et al., 2010
Xiagucheng	505	Qin et al., 2014
Kekeli	501	Wu et al., 2010

Niuxingshan	477	Wu et al., 2011
Niuxingshan	453	Wu et al., 2010
Leigongshan	453	Tseng et al., 2009
Gangcha	450	Wu et al., 2010
Dongjiazhuang	446	Yong et al., 2008
Shichuan	445	Wu et al., 2010
Lianhuashan	441	Zhang et al., 2017
Ophiolite		
Aoyougou	504-495	Tseng et al., 2007
Yushuigou	548-529	Song et al., 2013
Dachadaban	517-487	Song et al., 2014
Jiugequan	490-458	Xia et al., 2010
Biandukou	479	Song et al., 2013
Laohushan	448.5	Song et al., 2013

References

Chen, Y., Song, S., Niu, Y., Wei, C., 2014. Melting of continental crust during subduction ini- tiation: a case study from the Chaidanuo peraluminous granite in the North Qilian suture zone. Geochim. Cosmochim. Acta 132, 311-336. https://doi.org/10.1016/j.gca.2014.02.011

Peng, Y., Yu, S., Zhang, J., Li, S., Sun, D., Tong, L., 2017. Early Paleozoic arc magmatism and metamorphism in the northern Qilian Block, western China: A case study of Menyuan-Kekeli. Acta Petrologica Sinica 33, 3925–3941.

Qin, H., Wu, C., Wang, C., Li, X., Lei, M., Liu, C., Li, M., 2014. LA-ICP-MS zircon U-Pb dating and geochemical characteristics of high Sr/Y-type granite from Xigela, eastern Qilian area. Acta Petrologica Sinica 30, 3759-3771.

Song, S., Niu, Y., Su, L., Xia, X., 2013. Tectonics of the North Qilian orogen, NW China. Gondwana Research 23, 1378–1401.

Tseng, C.Y., Yang, H.J., Yang, H.Y., Liu, D., Wu, C., Cheng, C.K., Chen, C.H., Ker, C.M., 2009. Continuity of the North Qilian and North Qinling orogenic belts, Central Orogenic System of China: Evidence from newly discovered Paleozoic adakitic rocks. Gondwana Research 16, 285-293. https://doi.org/10.1016/j.gr.2009.04.003

Tseng, C.Y., Yang, H.J., Yang, H.Y., Liu, D.Y., Tsai, C.L., Wu, H.Q., Zuo, G.C., 2007. The

Dongcaohe ophiolite from the North Qilian Mountains: a fossil oceanic crust of

the Paleo-Qilian ocean. Chinese Science Bulletin 52, 2390–2401.
Wu, C., Gao, Y., Frost, B.R., Robinson, P.T., Wooden, J.L., Wu, S., Chen, Q., Lei, M., 2011. An early Palaeozoic double-subduction model for the North Qilian oceanic plate: evidence from zircon SHRIMP dating of granites. International Geology Review 53, 157-181. https://doi.org/10.1080/00206810902965346
Wu, C., Xu, X., Gao, Q., Li, X., Lei, M., Gao, Y., 2010. Early Palaezoic granitoid magmatism and tectonic evolution in North Qilian, NW China. Acta Petrologica Sinica 26, 1027-1044.
Xia, X.H., Song, S.G., 2010. Forming age and tectono-petrogenises of the Jiugequan ophiolite
in the North QilianMountain, NWChina. Chinese Science Bulletin 55, 1899–1907.
Zhang, L., Zhang, H., Zhang, S., Xiong, Z., Luo, B., Yang, H., Pan, F., Zhou, X., Xu, W., Guo, L., 2017. Lithospheric delamination in post-collisional setting: Evidence from intrusive magmatism from the North Qilian orogen to southern margin of the Alxa block, NW China. Lithos 288, 20-34. https://doi.org/10.1016/j.lithos.2017.07.009

1131